THE HONG KONG
POLYTECHNIC UNIVERSITY
香港理工大學

Department of Applied Physics

Design and Fabrication of Optical Tunable Filters

Lam Man Ying

A thesis submitted in partial fulfillment of the requirements for

the degree of Master of Philosophy

December 2013

CERTIFICATE OF ORIGINALITY

I hereby declare that this thesis is my own work and that, to the best of my knowledge and belief, it reproduces no material previously published or written, nor material that has been accepted for the award of any other degree or diploma, except where due acknowledgement has been made in the text.

_____ (Signed)

LAM MAN YING (Name of student)

Abstract

This research study aims to develop optical tunable filters (OTFs) for next-generation telecommunication networks and microfluidic systems using different tuning mechanisms. Two types of OTFs have been investigated: PZT-actuated OTF and electrolyte-capacitor (EC) OTF. The former utilizes a well established tuning method but tries to improve the specifications for practical industrial applications. The latter explores a new tuning mechanism and focuses more on scientific study.

The PZT-actuated OTF consists of two mirrors, each has high reflection (HR) coating (reflectivity > 95% over the C-band) in one surface and anti-reflection (AR) coating (reflectivity < 0.01%) on the other surface. One of the mirrors is attached to a miniature PZT actuator mounted on an L-shaped brass holder, while the other one is fixed to another brass holder directly. Tuning of the transmission wavelengths is achieved by applying a bias voltage to the PZT-actuator to change the cavity length.

In this project, 20 miniaturized tunable filters have been fabricated and packaged, with typical dimensions of $8 \times 5 \times 5$ mm^3, a wavelength shift of ± 1 nm/ V within the bias of ± 20 V, an insertion loss of 0.5 dB and a response time of 1 ms. The size is small enough to fit into the butterfly package box (25 mm × 10.7 mm × 9.5 mm) that houses the narrow-linewidth tuning laser developed for the industrial partner, and the tuning performance is superior to the available products. Moreover, the mechanical stability and the PZT hysteresis problem have been investigated in detail, and different designs of brass holders and packaging methods have been explored. To deal with the hysteresis problem between the voltage and the PZT displacement (displacement error > 20%), a

current injection actuation technique has been developed to reduce the error to < 2% in open loop. As a result, it simplifies the feedback control of laser wavelengths. The packaged OTFs have been successfully used in the butterfly-packaged narrow-linewidth tunable lasers, which demonstrated superior tunability and spectral purity.

On the scientific side, this research proposes a new tuning method – the electrolyte-capacitor method. This is accomplished by constructing the Fabry-Pérot etalon in a structure of electrolyte capacitor and by filling the FP cavity with ionic liquid. Under the bias voltage, the ion concentration and thus the refractive index of the ionic liquid could be tuned significantly. In the experiment, one of the mirror of the FP etalon (called electrode mirror) has half of its HR surface coated with a gold thin film, whereas the other mirror (called capacitor mirror) has half of its HR surface coated with a silver thin film covered by a layer of SiO_2. Then, both mirrors are put together with their coated parts facing each other, and the FP resonant cavity is filled with BMIM-PF_6 ionic liquid. In the FP etalon, the coated non-transparent half region is for electrical tuning and the uncoated transparent half region is for light propagation. At the beginning, the FP cavity only allows a comb of wavelength to pass through. When a bias voltage is applied to the coated parts, the electric field is built up across the SiO_2 layer; and ions are attracted to the capacitor side. As a result, the ion concentrations in the uncoated transparent region are reduced accordingly, leading to a change of the refractive index and thus the optical path length of the FP cavity. Therefore, the transmission peaks of the tunable filters are shifted. For experimental demonstration, we have fabricated the device and have obtained a wavelength shift at about 0.17 nm/ V within the bias 0–17 V. Apart from BMIM-PF_6, a varieties of electrolytes have

examined, including salt solution (NaCl) and conductive polymers (PEDOT and Nafion). BMIM-PF_6 solution presents the best performance in terms of insertion loss, contrast and tunability. Although the performance has a lot to be improved, this tunable filter demonstrates a new working principle and may be applicable to microfluidic systems that require on-chip optical filters in fluidic environment.

In conclusion, this research study has successfully developed two types of optical tunable filters, the PZT-actuated tunable filters and the electrolyte-capacitor tunable filters. For industrial applications, the PZT-actuated tunable filters have small dimensions, large tuning range, convenient electrical control, high speed and good linearity, and meet the stringent requirements of the narrow-linewidth tunable lasers under development for commercial uses in next-generation high-speed coherent communication networks. For scientific study, the electrolyte-capacitor (EC) tunable filters utilize a new mechanism and feature no mechanical movement and easy integration with microfluidic systems. All these help provide new tunable filters for telecommunication and microfluidic systems.

List of Publications

Peer-reviewed Journals

1. M. Y. Lam, N. Wang, D. Y. Lei and X. M. Zhang, Optofluidics tunable filters based on ionic liquid electrolyte capacitor, Optics Letters (submitted).

2. N. Wang, M. Feng, Z. Q. Feng, M. Y. Lam, L. Gao, B. Chen, A. Q. Liu, Y. H. Tsang and X. M. Zhang, Narrow-linewidth tunable lasers with retro-reflective external cavity, IEEE Photonics Technology Letters, vol. 24, no. 18, pp. 1591-1593, 2012.

Presentations in international conferences

1. M. Y. Lam and X. M. Zhang, "Electrolyte-tuned optical tunable filters", **ICMAT 2013, The 7th International Conference on Materials for Advanced Technologies**, Singapore, June 30 – July 5, 2013

2. M. Y. Lam and X. M. Zhang, "Optofludics tunable filters based on ionic liquid electrolyte capacitor", **The 3rd International Conference on Optofluidics 2013**, Hong Kong, August 15-17, 2013.

Academic Awards

1. **Best Poster Award**, The 7th International Conference on Materials for Advanced Technologies (ICMAT 2013), June 30 – July 5, 2013, Singapore, paper title: *Electrolyte-Tuned Optical Tunable Filters*, authors: M. Y. Lam, X.M. Zhang.

Acknowledgements

I would like to express my appreciation to my supervisor Dr. X. M. Zhang for his guidance and constant encouragement throughout the whole period of my research work.

Moreover, I feel really grateful to Dr. M. Feng, Dr. Z. Q. Feng, Mr. W. F. Cheng and Mr. N. Wang for the encouragement and technical support in design and fabrication of the devices and the feedback control circuit.

Furthermore, I appreciate the support of Material Research Center (MRC) of The Hong Kong Polytechnic University for the thin film fabrication. My gratitude goes to Dr. H. F. Lui, also to who teaches me the operation of sputtering machine and gives me very useful advices on thin film deposition.

The last but not least, I would like to thank my parents and friends for their patience, endless support, understanding and encouragement. They have been inspiring me at every moment.

Table of Contents

List of Figures

List of Tables

Chapter 1
Introduction

1.1 Objective

This research study aims to develop optical tunable filters (OTFs) using different tuning mechanisms for the applications of next-generation telecommunication networks and microfluidic systems. Two types of OTFs are to be investigated, PZT-actuated OTF and electrolyte-capacitor (EC) OTF. The former utilizes a well-known tuning method but tries to improve the specifications for real industrial applications. The latter explores a new tuning mechanism and focuses more on scientific study.

1.2 Motivation

Recent years have seen an increasing demand for high-speed telecommunication, especially for the internet-based entertainments such as movies watching, online games and website surfing. Therefore, the Dense Wavelength Division Multiplexing (DWDM) technique has been introduced to increase the transmission capacity by increasing the number of wavelength channels. In the commercial photonic network systems as shown in Fig. 1.1, 80-100 wavelength channels are multiplexed into one optical fiber for long-haul transmission. Each signal is carrier by one wavelength [1,2]. Tunable filters play a key role in such DWDM network systems. On the input side, the OTFs enable the tuning of laser wavelengths, and realize tunable lasers as the light sources. On the output side, the OTFs enable the demultiplexing of wavelength channels and select the

desired channels for optical detection. Therefore, the OTF is the enabling component of modern telecommunication networks.

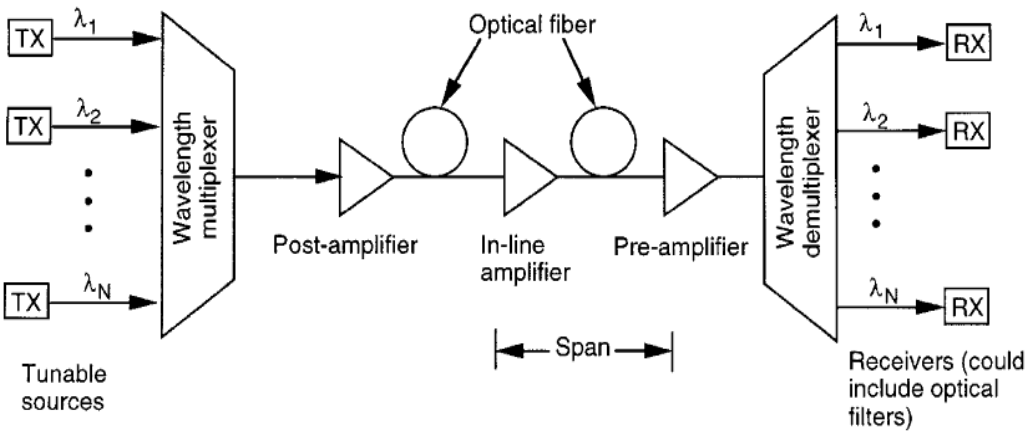

Fig. 1.1 Architecture of a DWDM system that makes use of multiple wavelength channels [3].

The use of tunable filters in the DWDM system as a demultiplexer is shown in Fig. 1.2. The incoming signals are carried by transmit the selected multiple frequencies from f_1 to f_N. A tunable filter is tuned to frequency f_i and blocks all the other unwanted channels. Similarly, the tunable filters can be used in many other optical devices or systems for wavelength selection.

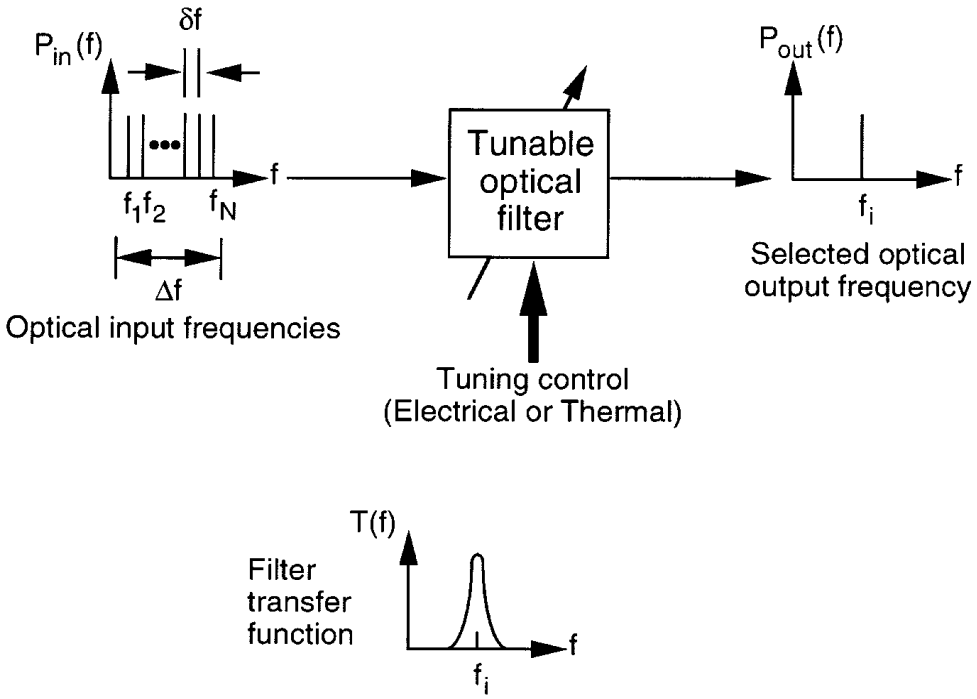

Fig. 1.2 Scenario of an optical tunable filter as a demultiplexer in a DWDM system [3].

Although the optical tunable filters have been extensively studied, there are still strong demands to develop new devices. On one hand, the rapid progress of telecommunication networks, especially the next-generation coherent communication systems, require new devices such as narrow-linewidth tunable lasers, in which the available optical tunable filters do not meet the requirements of dimensions or performance (e.g., linewidth, tuning speed). On the other hand, new tuning methods are worth exploring for new applications such as microfluidic systems and lab-on-a-chip devices. This research study answers these calls by developing miniaturized high-performance PZT-tuned optical filters and exploring the new tuning method using electrolyte-capacitor design.

1.3 Overview

In chapter 1, the objective and the motivation of this research are introduced.

In chapter 2, different interferometers and various tuning methods are reviewed. The interferometers such as fiber Bragg grating, Mach-Zehnder interferometer and Fabry-Pérot interferometer (FPI) provide the basic wavelength selection mechanisms for the optical tunable filters. Detailed discussions of the FPI specifications such as transmission spectrum, free spectral range, finesse, linewidth and contrast are provided as well. In addition, different tuning methods of tunable filters are presented, including thermal tuning, piezoelectric tuning and liquid crystal tuning.

In chapter 3, the working principle of the piezoelectric tunable filter (PZT-TF) based on the FPI is investigated. Also, experimental setup, fabrication procedures and device design of the PZT-TF are also elaborated.

In chapter 4, the experimental results and the characterization of the PZT tunable filter are described, including the tuning property, the peak shifting against bias and the dynamic response of the PZT-TF. In addition, the hysteresis and creeping problems of PZT-TF, caused by the PZT, are tackled by a charge drive method.

In chapter 5, the working principle of electrolyte-capacitor tunable filter (EC-TF) is studied. Moreover, the experimental setup and the design of the EC-TF are also

described. Furthermore, a theoretical modeling of EC-TF, including the simple model and a field model, are introduced for analyzing with the experimental results.

In chapter 6, the experimental results and characterization of EC-TF are presented, including the tuning property and the dynamic response of EC-TF. Four types of electrolyte solutions, filled in the FP cavity, are tested and compared.

In chapter 7, the important findings of two optical tunable filters, the PZT-TF and EC-TF are concluded and the recommended future work is suggested.

Chapter 2

Literature Review

As the background knowledge for tunable optical filters (OTF), this chapter will review different interferometers for wavelength selection in OTFs and will briefly discuss different tuning methods.

2.1 Fiber Bragg grating (FBG)

Fiber Bragg grating (FBG) is a popular design of optical filters as it is based on all fibers. To fabricate, a photomask having the specific periodic grating is put onto the photosensitive single mode fiber and is then exposed under ultraviolet light. The exposed parts of the fiber undergo a phase change and thus a slight change of refractive index. As a result, the fiber carries a periodic modulation of the refractive index in the length direction (see Fig. 2.1). When the light goes through the FBG, it reflects a wavelength but transmits all others. The specific Bragg wavelength follows:

$$\lambda_B = 2\eta_e \Lambda \tag{2.1}$$

where λ_B is Bragg wavelength, Λ is the grating period, and η_e is the effective refractive index of the grating in the fiber core.

Since the grating period and the effective refractive index of grating are dependent on temperature and strain, the Bragg wavelength can be tuned by varying the temperature or varying the strain of the FBG (see Fig. 2.2). It is noted that the

wavelength peak appears in the reflection. This is different from the next two types of interferometers to be introduced, in which the peaks appear in the transmission.

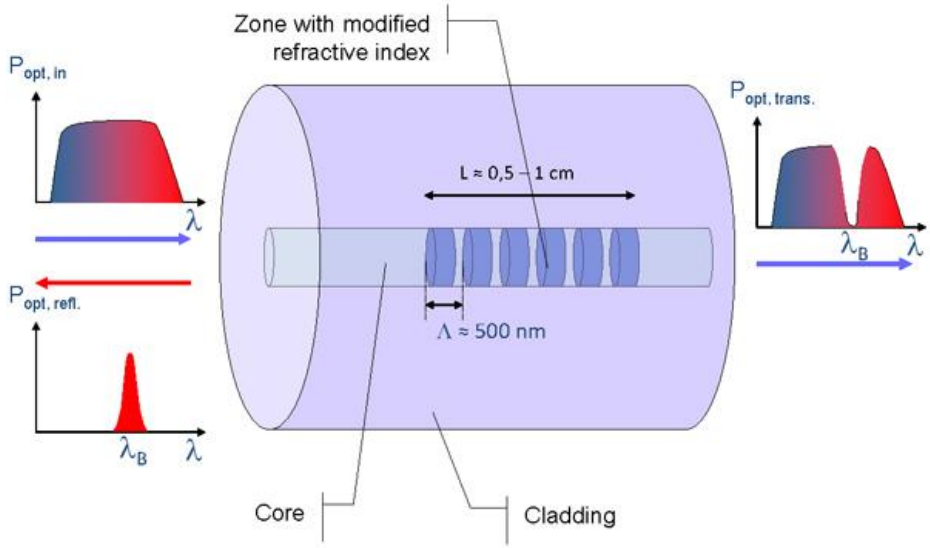

Fig. 2.1 Basic working mechanism of fiber Bragg grating (FBG) [4].

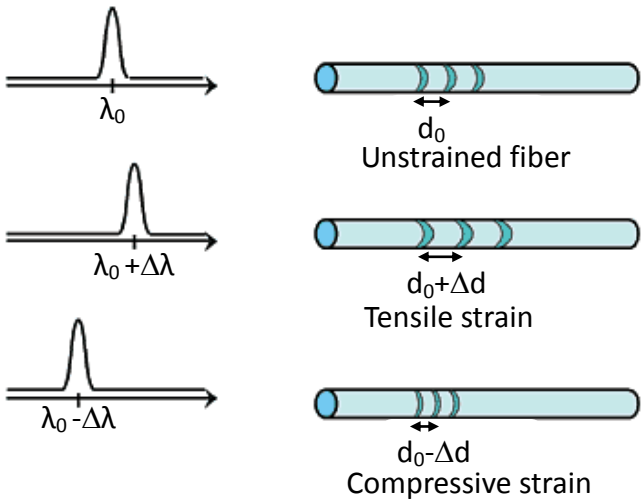

Fig. 2.2 Shifting of central wavelength under different strains [5].

2.2 Mach-Zehnder interferometer (MZI)

A Mach-Zehnder interferometer (MZI) consists of two optical beams with different optical path lengths and a phase shift element which is represented by a tuning element

in Fig. 2.3. When light is transmitted into the MZI, it is divided into two arms by an optical coupler. After a bias is applied to one arm of the MZI, one of the light beams is delayed. When the two light beams are merged by the other coupler, they interfere with each other to select the wavelengths for transmission [6-8].

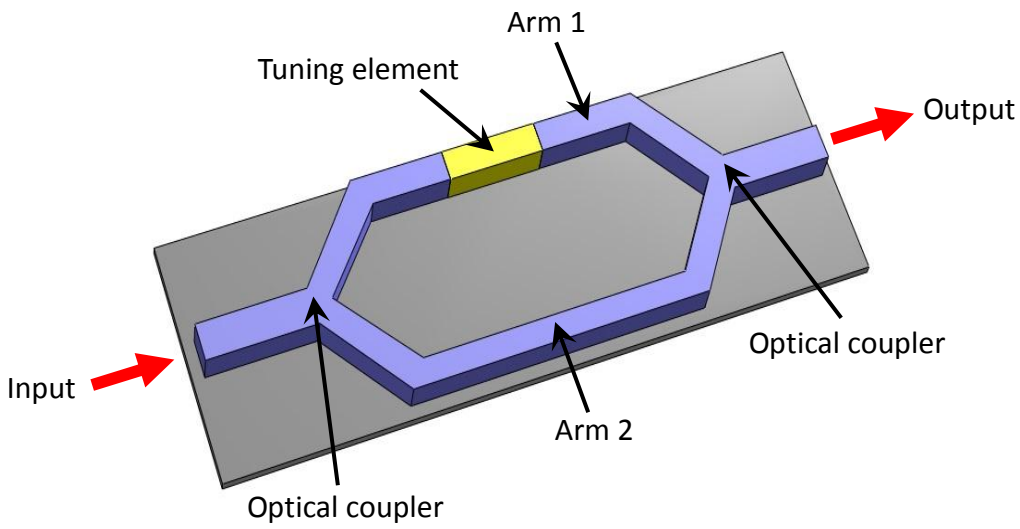

Fig. 2.3 Structure of Mach-Zehnder interferometer [9].

2.3 Fabry-Pérot interferometer (FPI)

The Fabry-Pérot interferometer (FPI) is based on multi-beam interference. It consists of two highly-reflective mirrors, which are aligned parallel to each other (see Fig. 2.4). Once the light beam hits the front mirror and is reflected back and forth between the surfaces of two mirrors, the transmitted lights interfere with themselves, and produce constructive and destructive interference (Fig. 2.4)

However, only particular wavelengths of light can resonate in the FP cavity, the conditions are:

$$m\lambda_0 = OPL = 2n_0L_0 \tag{2.2}$$

$$\frac{\Delta\lambda}{\lambda_0} = \frac{\Delta n}{n_0} + \frac{\Delta L}{L_0} \tag{2.3}$$

where m refers to an integer, λ_0 refers to resonant wavelength, L_0 refers to the FP cavity length, n_0 refers to the refractive index of material in the FP cavity, OPL refers to the optical path length of FPI.

When the condition (2.2) is satisfied, the light of the specific wavelength is built up in the resonant cavity and is transmitted out of the FPI. This generates a pattern of circular fringes on the screen. In addition, based on the condition (2.3), the tuning of the FPI can be done by either varying the length of FP cavity (i.e., using a piezoelectric actuator) or the refractive index of material in the FP cavity (i.e., using liquid crystal elements to alter its refractive index).

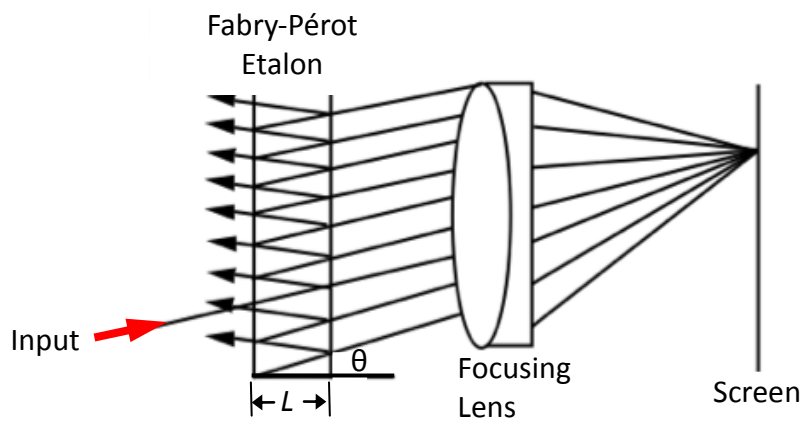

Fig. 2.4 Fabry-Pérot interferometer using multi-beam interference [10].

2.3.1 Transmission spectrum of FPI

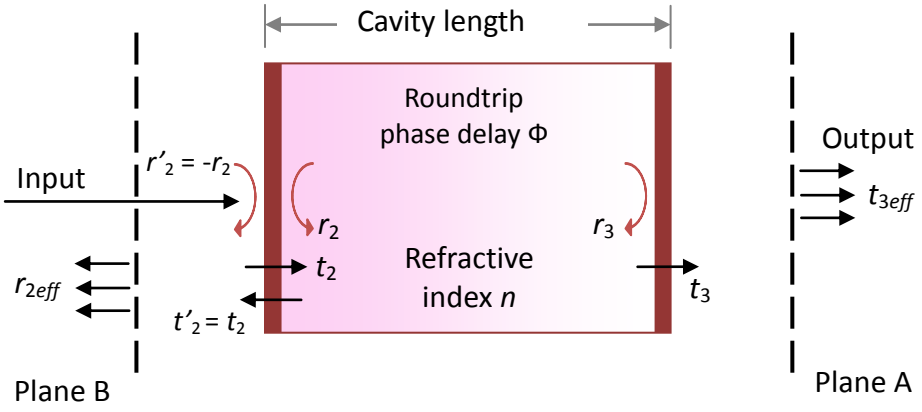

Fig. 2.5 Transmission and reflection in Fabry-Pérot interferometer.

The transmission spectrum is the most important feature of the FPI and it is thus derived here in details. The derivation below is based on the assumptions that:

- All the reflection surfaces are dielectric, i.e., r_2, r_3, t_2 and t_3 are all real, $R_2 = r_2^2, R_3 = r_3^2, t_2^2 = T_2 = 1 - R_2, t_3^2 = T_3 = 1 - R_3$. Here r_2 and t_2 refer to the reflection and transmission at the input plane, r_3 and t_3 refer to the reflection and transmission at the output plane as indicated in Fig. 2.5.
- By the Stokes relation, the reflection and transmission are independent of the directions, i.e., $r_2^{'} = -r_2$ and $t_2^{'} = t_2$. $r_2^{'}$ and $t_2^{'}$ are the reflection and transmission as indicated in Fig. 2.5.

The input light beam passes through the etalon directly:

The 0th run transmission: $$t_2 e^{j\frac{\Phi}{2}} (r_2 e^{j\Phi} r_3)^0 t_3 \qquad (2.4a)$$

here Φ is the phase delay of roundtrip as given by

$$\Phi = \frac{4\pi nL}{\lambda}$$

where n and L are the refractive index and the physical length of the cavity, respectively. λ is the wavelength of light beam.

After the light beam goes into the etalon, it undergoes the 1st roundtrip and a phase change:

The 1st run transmission: $$t_2 e^{j\frac{\Phi}{2}} (r_2 e^{j\Phi} r_3)^0 (r_2 e^{j\Phi} r_3) t_3 \tag{2.4b}$$

And the 2nd, 3rd… to nth multiple roundtrip occur in the FP etalon:

The 2nd run transmission: $$t_2 e^{j\frac{\Phi}{2}} (r_2 e^{j\Phi} r_3)^0 (r_2 e^{j\Phi} r_3)(r_2 e^{j\Phi} r_3) t_3$$

$$= t_2 e^{j\frac{\Phi}{2}} (r_2 e^{j\Phi} r_3)^2 t_3 \tag{2.4c}$$

The 3rd run transmission: $$t_2 e^{j\frac{\Phi}{2}} (r_2 e^{j\Phi} r_3)^0 (r_2 e^{j\Phi} r_3)(r_2 e^{j\Phi} r_3)(r_2 e^{j\Phi} r_3) t_3$$

$$= t_2 e^{j\frac{\Phi}{2}} (r_2 e^{j\Phi} r_3)^3 t \tag{2.4d}$$

The nth run transmission: $$t_2 e^{j\frac{\Phi}{2}} (r_2 e^{j\Phi} r_3)^n t_3 \tag{2.4e}$$

By the observation in plane A, the effective transmission can be represented by

$$t_{3eff} = t_2 e^{j\frac{\Phi}{2}} (r_2 e^{j\Phi} r_3)^0 t_3 + t_2 e^{j\frac{\Phi}{2}} (r_2 e^{j\Phi} r_3) t_3 + t_2 e^{j\frac{\Phi}{2}} (r_2 e^{j\Phi} r_3)^2 t_3$$

$$+ t_2 e^{j\frac{\Phi}{2}} (r_2 e^{j\Phi} r_3)^3 t_3 + \ldots + t_2 e^{j\frac{\Phi}{2}} (r_2 e^{j\Phi} r_3)^n t_3$$

$$t_{3eff} = \sum_{k=0}^{n} t_2 e^{j\frac{\Phi}{2}} (r_2 e^{j\Phi} r_3)^k t_3 \tag{2.5}$$

By using $\sum_{k=0}^{n} ar^k = a\left(\frac{1-r^{n+1}}{1-r}\right)$, the effective transmission is

$$t_{3eff} = \sum_{k=0}^{n} t_2 e^{j\frac{\Phi}{2}} t_3 \left(\frac{1-(r_2 e^{j\Phi} r_3)^{n+1}}{1-r_2 e^{j\Phi} r_3}\right) \approx \frac{t_2 e^{j\frac{\Phi}{2}} t_3}{1-r_2 e^{j\Phi} r_3} \quad \text{If } n\to\infty \text{ and } |r_2 r_3| < 1 \tag{2.6}$$

The intensity of transmission is

$$T_{3eff} = |t_{3eff}|^2 = \left|\frac{t_2 e^{j\frac{\Phi}{2}} t_3}{1-r_2 e^{j\Phi} r_3}\right|^2 = \frac{(t_2 t_3)^2}{1-2r_2 r_3 \cos\Phi + (r_2 r_3)^2} \tag{2.7}$$

From the previous assumptions, Eq. (2.7) can be expressed as

$$T_{3eff} = \frac{(1-R_2)(1-R_3)}{1-2\sqrt{R_2 R_3}\cos\Phi + R_2 R_3} \tag{2.8}$$

In case, the reflectivities of mirrors in the etalon are equal,

$$r_2 = r_3 = r, \quad \text{then,} \quad R_2 = R_3 = R,$$

$$T_{3eff} = \frac{(1-R)^2}{1-2R\cos\Phi + R^2} \tag{2.9}$$

Moreover, it can be expressed as

$$T_{3eff} = \frac{1}{1+F\sin^2\frac{\Phi}{2}} \tag{2.10}$$

where F is the coefficient of finesse as defined by

$$F = \frac{4R}{(1-R)^2} \tag{2.11}$$

From Eq. (2.9), it can be seen that the transmission spectrum is determined by the mirror reflectivity R and the phase delay Φ. Below we will study the FPI performance using different reflectivities and different cavity lengths.

2.3.1.1 Influence of mirror reflectivity

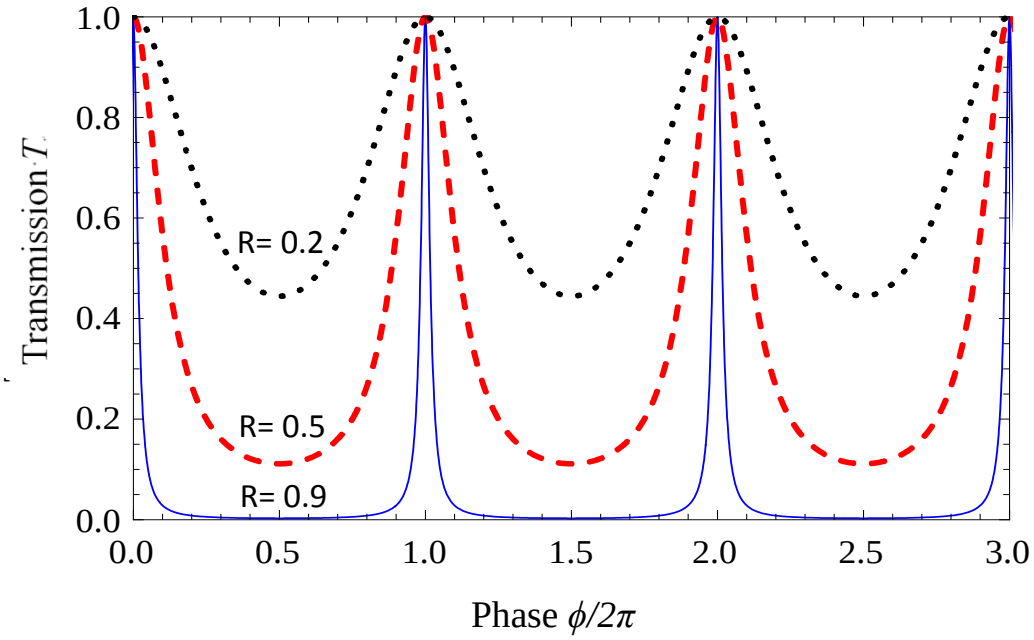

Fig. 2.6 Influence of the transmission spectrum by the reflectivity of mirrors.

Transmission spectra for R = 0.2, 0.5 and 0.9 are plotted in Fig. 2.6. For lossless mirrors, the maximum transmission always reaches 1 when $\phi=2m\pi$ (where m refers to an integer), regardless of the value of R. However, the minimum transmission T_{min} is dependent on R. Higher R gets a smaller T_{min} and thus a better contrast (to be discussed later).

2.3.1.2 Influence of cavity length

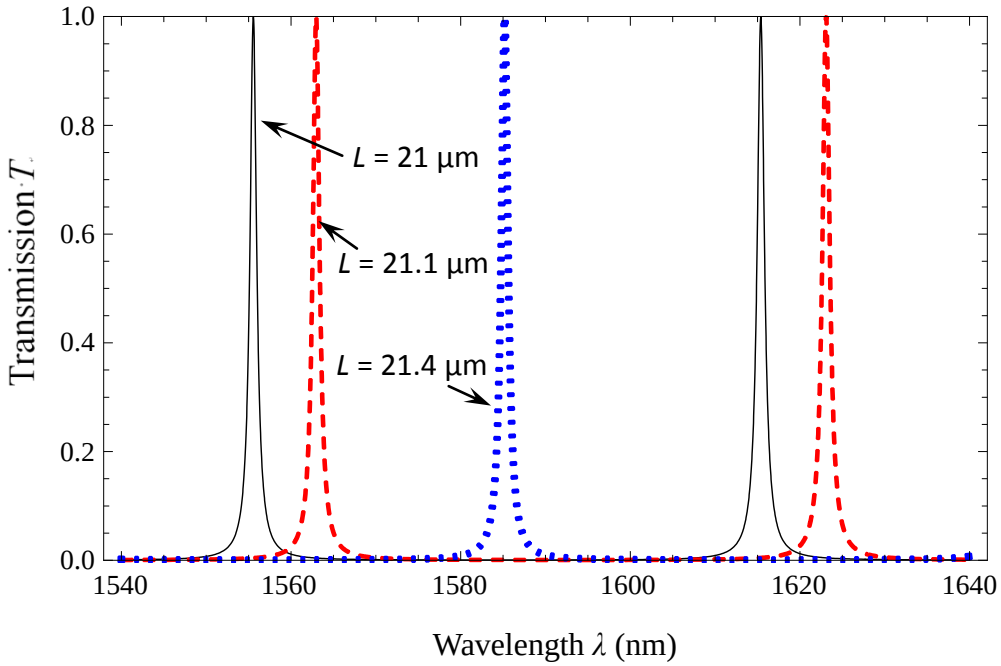

Fig. 2.7 Transmission spectra of the FPI with R=0.95.

The transmission spectrum is dependent on the roundtrip phase delay, which is in turn determined by the optical path length (OPL) of FP cavity. As the OPL is the product of refractive index and the resonant cavity, the phase delay can be changed equivalently by the refractive index or the cavity length. For simplicity, we assume that the refractive index is fixed and plot the transmission spectra at different cavity lengths in Fig. 2.7. It can be seen that when the cavity length is increased from 21 to 21.1 μm, the transmission peaks are shifted to longer wavelengths, which agrees with Eq. (2.2). When L is further increased to 21.4 μm, the peaks will be shifted further to even longer wavelengths.

2.3.2 Important specifications of FPI

Several important parameters are essential for the FPI, for example, insertion loss, free spectral range (FSR), linewidth, finesse and contrast ratio [11]. Below we will study them one by one.

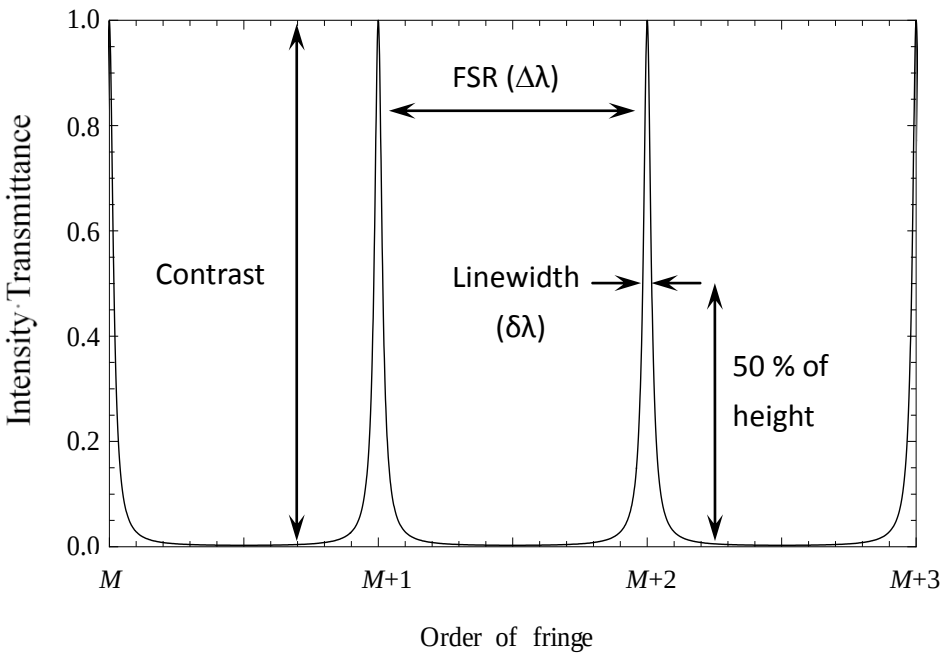

Fig. 2.8 Transmission spectrum of an FP etalon.

2.3.2.1 Free spectral range (FSR)

The free spectral range (FSR) of the FPI is the frequency or wavelength spacing between two successive transmitted peaks. It determines the tuning range of the optical filter [12]. Considering two successive transmitted peaks, *M* and *M*+1 in Fig. 2.8, the relationship between FSR and the position of transmittance fringe can be expressed by

$$\lambda_M = \frac{2nL}{M} \tag{2.12a}$$

$$\lambda_{M+1} = \frac{2nL}{M+1} \tag{2.12b}$$

$$\Delta\lambda = \lambda_M - \lambda_{M+1} = \frac{2nL}{M} - \frac{2nL}{M+1} \tag{2.13a}$$

$$\Delta\lambda = \frac{2nL}{M}\left(\frac{1}{M+1}\right)$$

$$\Delta\lambda = \frac{\lambda_M}{M+1}$$

$$\Delta\lambda = \frac{\lambda_M \lambda_{M+1}}{2nL} \tag{2.13b}$$

For the FPI with narrow spacing, $\lambda_M \approx \lambda_{M+1} \approx \lambda$, therefore

$$\Delta\lambda = \frac{\lambda^2}{2nL} \tag{2.14}$$

It reveals that an increase of the cavity length would cause a decrease of FSR.

2.3.2.2 Contrast ratio

From Eq. (2.10), the maximum transmission T_{max} and the minimum transmission T_{min} can be expressed as

$$T_{\max} = 1 \tag{2.15}$$

$$T_{\min} = \frac{1}{1+F} \tag{2.16}$$

The contrast ratio (CR) is defined as

$$CR = \frac{T_{\max} - T_{\min}}{T_{\max} + T_{\min}} \tag{2.17a}$$

In the ideal case,

$$CR = \frac{F}{2+F} = \frac{2R}{1+R^2} \tag{2.17b}$$

And the contrast is defined as

$$C_t = 10\log_{10}\frac{T_{\max}}{T_{\min}} \tag{2.18a}$$

In the ideal case,

$$C_t = 10\log_{10}(1+F) \tag{2.18b}$$

2.3.2.3 Linewidth of full width at half maximum (FWHM)

Based on Eqs. (2.15) and (2.16), half maximum of the transmission:

$$T_{0.5} = \frac{1}{2}\left(T_{\max} + T_{\min}\right) = \frac{2+F}{2+2F} \tag{2.19}$$

From Eq. (2.10), the phase $\Phi_{0.5}$ at half maximum should satisfy

$$\frac{1}{1+F\sin^2\frac{\Phi_{0.5}}{2}} = \frac{2+F}{2+2F} \tag{2.20}$$

$$\Phi_{0.5} = \pm 2\arcsin\left(\frac{1}{\sqrt{2+F}}\right) \tag{2.21}$$

As the phase delay follows $\Phi = \frac{4\pi nL}{\lambda}$, then

$$\delta\Phi = \frac{4\pi nL}{\lambda^2}\delta\lambda \tag{2.22}$$

$$\delta\lambda = \frac{\lambda^2}{4\pi nL}\delta\Phi$$

$$= \frac{\lambda^2}{\pi nL}\arcsin\left(\frac{1}{\sqrt{2+F}}\right) \tag{2.23}$$

here $\delta\lambda$ is the linewidth of full width at half maximum (FWHM).

2.3.2.4 Finesse

The finesse F_i is defined as

$$F_i = \frac{\Delta\lambda}{\delta\lambda} \tag{2.24}$$

$\Delta\lambda$ is the FSR and $\delta\lambda$ is the linewidth. From Eqs. (2.14) and (2.23), then

$$F_i = \frac{\Delta\lambda}{\delta\lambda} = \frac{\pi}{2\arcsin\left(\frac{1}{\sqrt{2+F}}\right)} \tag{2.25}$$

For high reflectivity, it has $F_i >> 1$ (e.g. R = 0.95 gives F_i =61.2), the above equation can be simplified into

$$F_i = \frac{\Delta\lambda}{\delta\lambda} = \frac{\pi\sqrt{R}}{1-R} \tag{2.26}$$

and the higher the reflectivity of mirrors is, the higher the finesse of FP etalon is (see Fig. 2.9).

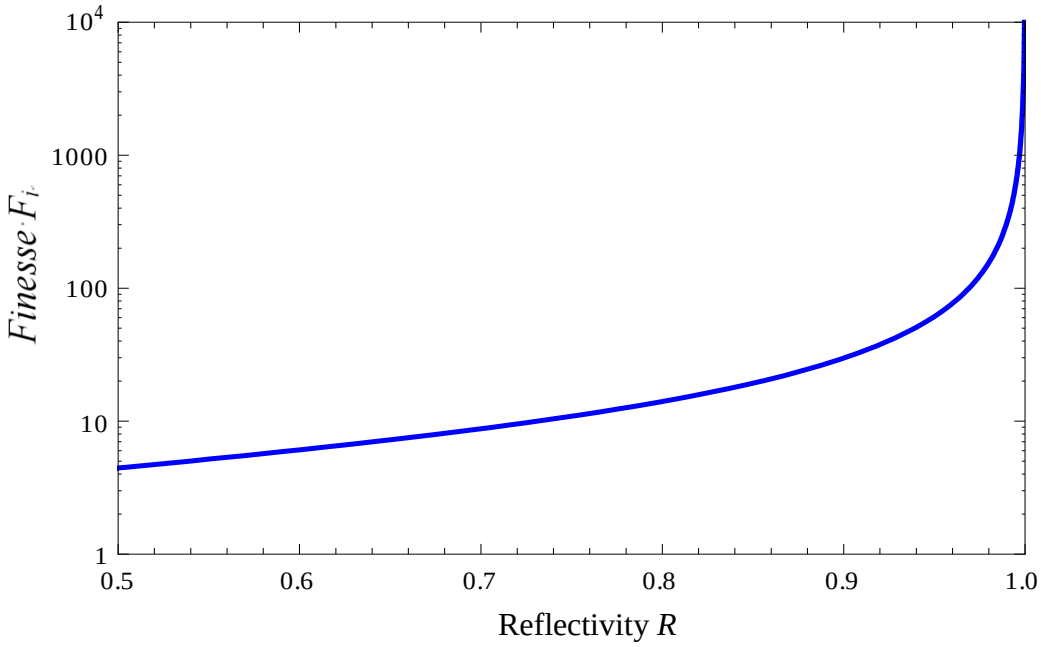

Fig. 2.9 Finesse as a function of the reflectivity of mirror.

2.3.3 Comparison between two-beam and multi-beam interferences

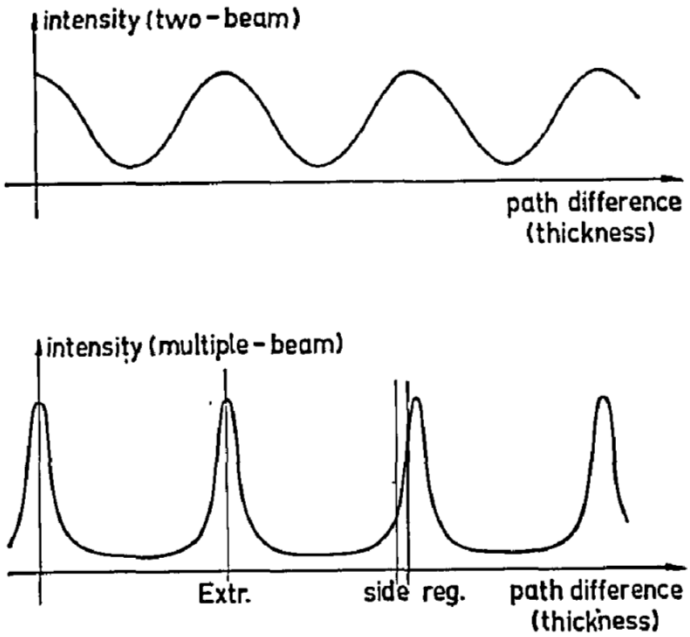

Fig. 2.10 Comparison of the intensity distributions of the two-beam and the multi-beam interference [13].

Generally speaking, the transmission fringes obtained from the multi-beam interference is much sharper than those from the two-beam interference. In the case of two-beam interference such as the MZI, the fringes are formed by the superposition of two waves. Therefore, the fringes follow a cosine relation as given by [14,15].

$$I = A^2 \tag{2.27}$$

$$I(x, y) = I_1 + I_2 + 2\sqrt{I_1 I_2}\cos(\Phi_1 - \Phi_2) \tag{2.28}$$

where I is the irradiance, I_1 and I_2 are the maximum and minimum transmission intensity, A is the amplitude, Φ is the phase of the wave, and Φ_1- $\Phi_2 = \Delta\Phi$ is the phase difference between the test and reference beams.

In case of multi-beam interference, such as the FBG and the FPI, the fringes are formed by the superposition of multiple waves. In the FBG, the reflection at every phase-changed region generates a beam for interference. In the FPI, each partially transmitted wave when the light beam bounces back and forth in the resonant cavity generates a beam for superposition.

The larger the number of the superimposed beams is, the stronger the interference becomes and thus the sharper the fringes are [16]. Therefore, to get a narrow-linewidth filter, the multi-beam interference based the FBG and the FPI are superior to the two-beam interference based the MZI. For the FBG and the FPI, the FPI is more suitable for narrow linewidth because of the use of highly-reflective mirrors.

2.3.4 Different tuning methods

In the past few decades, various tuning methods have been developed for the OTFs, especially for industrial applications. Most of them utilize the FPI structure and follow the working mechanism of changing either the cavity length or the refractive index of medium in the FP cavity, ultimately varying the OPL of OTF [3,17,18]. For instance, the thermal tuning method varies the temperature to change the OPL of FP cavity [19-21]; the piezoelectric tuning method applies a bias voltage on the PZT actuator to change the cavity length of OTF [22,23]; the liquid crystal (LC) tuning method applies a bias voltage to change the refractive index of the LC element [24-27]. The table below summarizes three different tuning methods.

Table 2.1 Different tuning methods for optical tunable filters.

Type of tunable filters (TFs)	Tuning methods	Tuning speed
Thermally tuned TF	Thermo-optic effect	> 10 ms
PZT TF	Piezoelectric effect	1-10 ms
Liquid crystal TF	Crystal orientation effect	0.5 - 10 μs

2.3.4.1 Thermal tuning

A typical design of OTF that uses the thermal tuning method is shown in Fig. 2.11. It consists of multilayer of quarter-wavelength high-index and low-index dielectric coatings, and forms two distributed Brag reflectors (DBRs). The FP cavity is made of a thick thermo-optic film between the two DBRs [28,29]. When a light beam is incident on the thin film OTF, the waves go inside the cavity and interfere constructively or destructively, therefore only the resonant wavelengths can be transmitted. The unwanted wavelengths are reflected off. Tuning of the wavelength can be achieved by heating up the thermo-optic material of the thick film in the FP cavity.

$$\frac{\Delta\lambda}{\lambda} = \Delta T\left(\alpha + \frac{1}{n}\frac{dn}{dT}\right) \tag{2.29}$$

where T is the temperature in Kelvin, α is the thermal expansion coefficient of the cavity material, and $\frac{dn}{dT}$ is the thermo-optic coefficient of material.

This thin film tunable filter typically has a high finesse and a linewidth of ~ 1 nm, and a tuning range up to 50 nm. However, it has the main drawback of slow response time due to the heat dissipation problem.

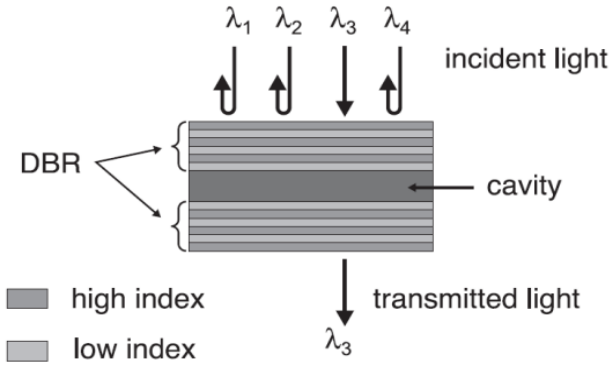

Fig. 2.11 Structure of thermally-tuned tunable filter [29].

2.3.4.2 Piezoelectric tuning

Basically, the piezoelectric tunable filter consists of two highly reflective mirrors and a PZT actuator (see Fig. 2.12). The two highly reflective mirrors are adjusted to be parallel and form a FP cavity. One of the mirrors is attached onto a PZT actuator for tuning and the other mirror is fixed. When a driving voltage is applied to the PZT, it alters the length of FP cavity. In addition, the PZT actuator compresses under a positive bias and extends under a negative bias (Fig. 2.13). As a result, the OPL can be increased or decreased. The tuning relation follows:

$$\frac{\Delta\lambda}{\lambda} = \frac{\Delta L}{L_0} \tag{2.30}$$

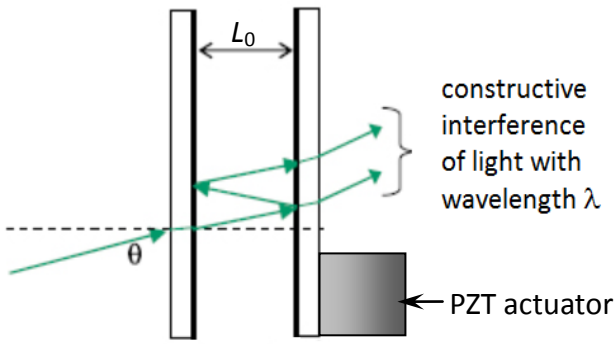

Fig. 2.12 Structure of piezoelectric tunable filter.

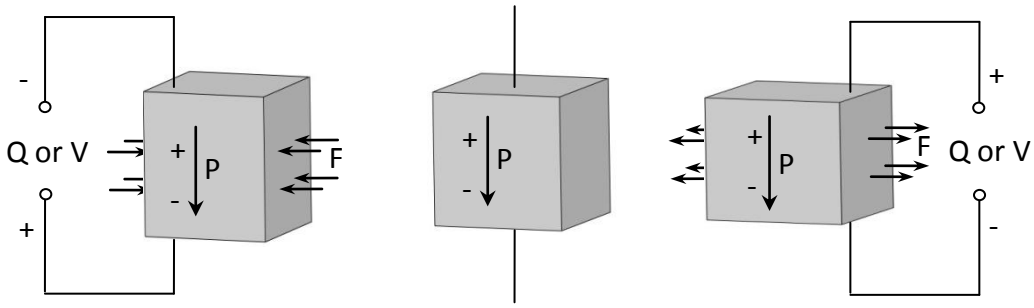

Fig. 2.13 PZT actuator when a bias is applied [30].

The PZT tunable filters inherit the merits of high finesse and narrow linewidth and may offer large tuning range. However, it involves mechanical movement, and may affect the parallelism of mirrors during tuning. Moreover, the PZT has the hysteresis and creeping problems using the voltage driving. These problems will be solved using the charge driving method (to be discussed in Chapter 4).

2.3.4.3 Liquid crystal tuning

Liquid crystals have three most common phases: nematic, smectic and chiral. In the liquid crystal tunable filters (LC-TF), nematic phase liquid crystal is commonly used [31-33]. It is a birefringent material whose refractive indices are dependent on the polarization and the propagation direction of light. The crystal orientation pattern can be influenced by either applying an electric field or a magnetic field (see Fig. 2.14). As a result, the refractive index is tuned for the light with a fixed polarization and a fixed propagation direction.

An OTF can be obtained by filling the liquid crystal into the FP cavity. A typical

design is shown in Fig. 2.15. Thus, the tuning can be achieved by modulating the refractive index of the liquid crystal. The relationship follows:

$$\frac{\Delta\lambda}{\lambda} = \frac{\Delta n}{n_0} \tag{2.31}$$

The liquid crystal tuning has many advantages, such as fast speed, and low loss. However, it has a serious drawback — the polarization dependence. It is not suitable for polarization sensitive systems. Moreover, high bias voltage is required for a large tuning range. It may damage the other components if the voltage is too high.

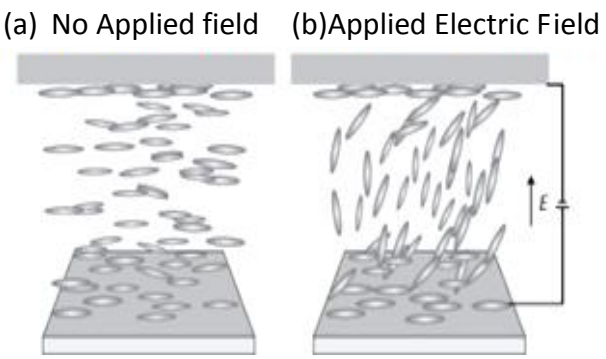

Fig. 2.14 Tuning of liquid crystal molecular orientation. (a) No electric field is applied. (b) Electric field is applied.

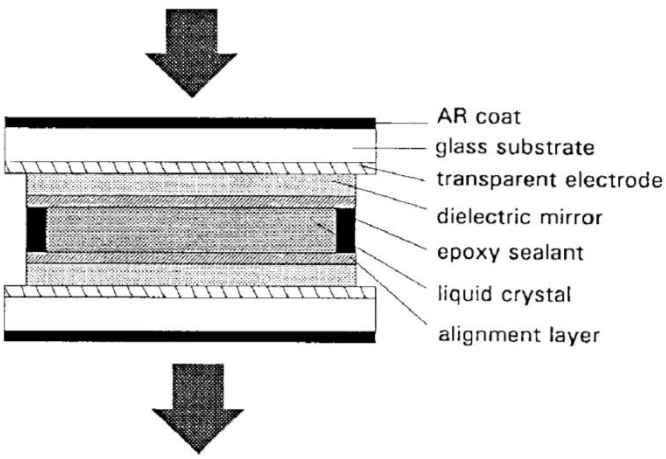

Fig. 2.15 Schematic diagram of a liquid crystal tunable filter [32].

2.4 Electrolyte capacitor

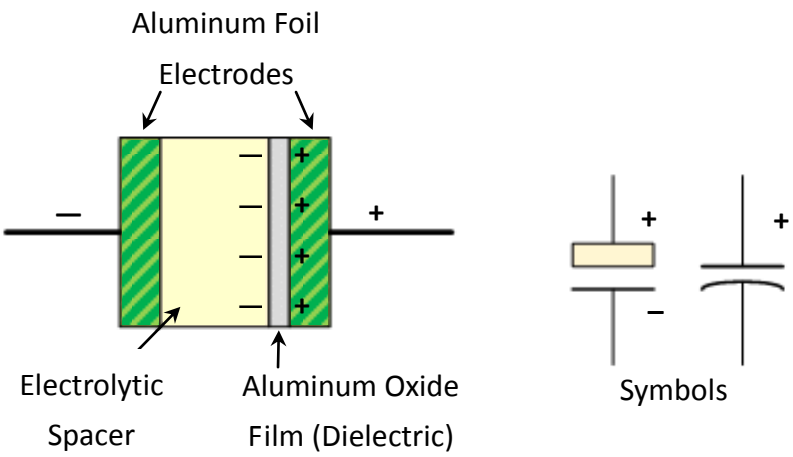

Fig. 2.16 Structure of an aluminum electrolyte capacitor [34].

In general, an electrolytic capacitor (EC) consists of two conductive metals that are separated by an extremely thin dielectric layer and an electrolyte solution. Here is an example of electrolyte capacitor (see Fig. 2.16). It has very thin layer of aluminum oxide film deposited on the aluminum (Al) foil electrode. This oxide layer serves as the dielectric thin film. The capacitance is expressed as

$$C = \varepsilon_r \varepsilon_0 \frac{A}{d} \tag{2.32}$$

where C is the capacity of the capacitor (capacitance), A is the area of the dielectric thin film, d is the thickness of dielectric thin film, ε_r is the relative static permittivity, and ε_0 is the permittivity of vacuum.

When the voltage is applied, large amount of electric charges are stored on the oxide thin film. As the capacitance is inversely propositional to the thickness of

dielectric thin film, therefore the thinner the oxide film is, the higher the capacitance can be obtained, and the more the charges can be stored.

In the second part of my research work, an electrolyte-capacitor tunable filter is fabricated based on this structure by altering the ion concentration of the electrolyte solution so as to tune the central wavelength. In Chapter 5 and 6, the working principle and the experimental results of the EC-TF will be elaborated.

2.5 Electrochromic window using ionic liquid

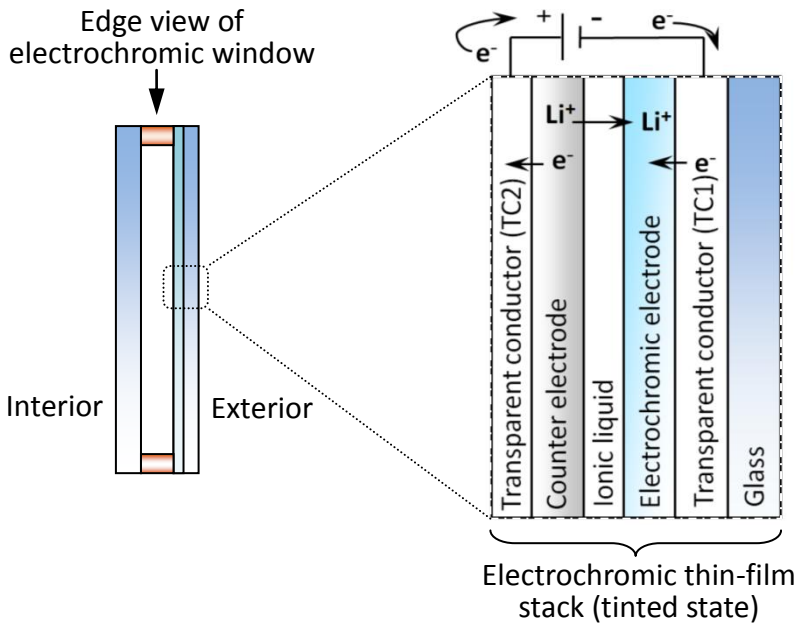

Fig. 2.17 Structure and working principle of electrochromic window [35].

The electrochromic window consists of two glazings, and one of the glazing consists of 5 layers as shown in Fig. 2.17. The wording “electrochromic” means when the material is energized by electric current, the color of the material will be changed. The electrochromic layer and counter electrode are separated by ionic liquid. The three

major layers are struck in between the transparent conductor layers (TC1&TC2). The coating of this glazing is used to reject the incoming solar radiation when the window is tinted and it transmits the incident light when the window is in clear state. When a small bias is applied between TC1 and TC2, the lithium ions (Li^+) stored in the counter electrode start to migrate through the ion conductor into the electrochromic layer. It then undergoes a gradual transition to change the color of window from clear to blue/grey. Once the bias voltage is removed, the Li^+ ions are moved back to the counter electrode. Thus, the window returns to the original clear state.

Chapter 3
Design and Fabrication of Piezoelectric Tunable Filters

In this chapter, the working mechanism of the piezoelectric tunable filters will be discussed and the procedures of fabrication will also be described.

3.1 Working principle of piezoelectric tunable filters

In the first part of this research, a piezoelectric tunable filters (PZT-TF) is fabricated. It consists of two mirrors with the highly refractive facets facing to each other, forming effectively a Fabry-Pérot (FP) cavity (see Fig. 3.2). When the input light beam hits the front mirror, partial light is reflected and the rest is transmitted to the rear mirror; at the rear mirror, part of the light is reflected and the rest is transmitted out of the rear mirror. The transmitted light beams form multiple resonances inside the FP cavity interfere with each other, allowing only certain wavelengths to have high transmission.

One of the mirrors is fixed while the other is attached to a piezoelectric transducer. The tuning is achieved by changing the gap between two mirrors using the PZT actuator. Under a positive voltage, the PZT actuator compresses, and thus the OPL increases; while a negative voltage is applied, the OPL decreases.

3.2 Visual estimation of the parallelism of mirrors

The parallelism of two mirrors in the FPI tunable filters is a critical condition for the proper operation of the tunable filters. The interference patterns provide a useful clue to visual estimation of the parallelism.

For a sodium light source, the path difference Δ, between the two interfering rays reflected by mirror 1 and mirror 2 at point P (see Fig. 3.1), could be expressed as

$$\Delta = n(AB + BC) - n'(AP - CP) \tag{3.1}$$

where n is the refractive index between mirrors, n' is the refractive index of mirror, d is the separation between mirrors, i_1 is the incident angle, i_2 is the refraction angle at point A, λ is the wavelength.

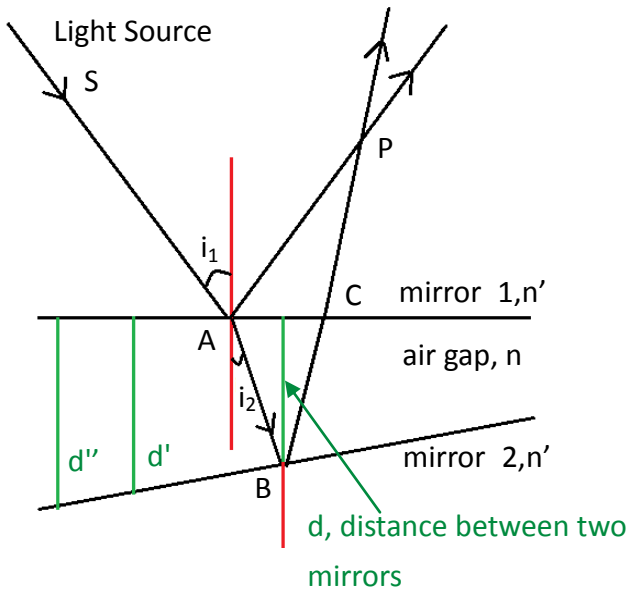

Fig. 3.1 Interference on point P of a wedge plate.

Considering the phase shift of the sodium light from source S at the surfaces of two mirrors, the path difference could be represented by

$$\Delta = 2nd\cos i_2 + \frac{\lambda}{2} \tag{3.2}$$

Optical path difference depends on the mirror separation and the refraction angle of incident light at A. For equal separation between mirrors, optical path difference is the same. In other words, any position on the mirror has the equal separation with the other mirror and would produce the same interference pattern. This phenomenon is known as the fringes of equal thickness [13]. Thus, the parallelism between mirrors could be obtained by observing the constructive interference patterns. This technique is adopted in our experiment for mirror alignment.

3.3 Design and fabrication

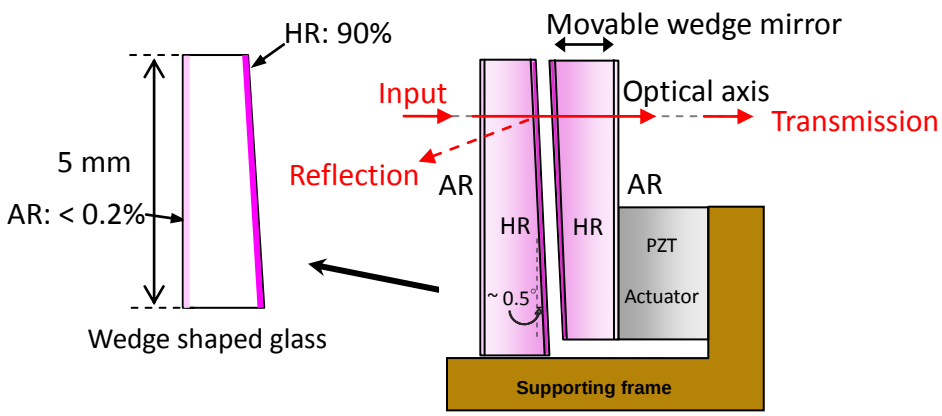

Fig. 3.2 Design of PZT tunable filters and specification of the wedge mirror.

For the PZT TF, the conceptual design is shown in Fig. 3.2 and the structural design and fabrication procedures are depicted in Fig. 3.2. Here two wedge mirrors with a tilting angle of 0.5^{o} are used. The small angle helps reflect the unwanted reflected light out of the optical axis [23,36]. As a result, only the transmitted light remains along the optical axis. This is important when the TF is inserted into the laser cavity. It ensures

only the transmission spectrum is used for the laser wavelegnth selection. Otherwise, the reflection spectrum of the TF would affect the wavelength selection too.

In the structural design, a piece of wedge-shaped mirror is fixed on a copper frame while the other piece of wedge-shaped mirror is fixed on an L-shaped copper frame through the PZT actuator (Fig. 3.3(a)). Then, two mirrors with copper frames are put together and adjusted with the HR facets facing to each other (Fig. 3.3(b)). Sodium lamp (λ = 589 nm) is used as a monochromatic light source to illuminate the mirrors. The shape of interference patterns can be used to estimate the level of parallelism between two HR facets. When two facets are in parallel, the separation of adjacent dark fringes would be very wide. Therefore, two facets are considered to be parallel when the dark fringes disappear. As the mirror is about 5 mm, one interference fringe over the whole mirror area corresponds to a parallelism of $\frac{\lambda}{5} \cong 6.7 \times 10^{-3}\,\mathrm{deg}$. After that, the transmission spectrum of the filters is measured by a broadband light source near 1.55 μm. The distance between the two HR facets can be adjusted to about 20 μm by observing the FSR to reach about 60 nm on the OSA. Finally, the two frames are joined by applying the quick-drying 415 glue to the region as indicated by the blue dashed line in Fig. 3.3(c).

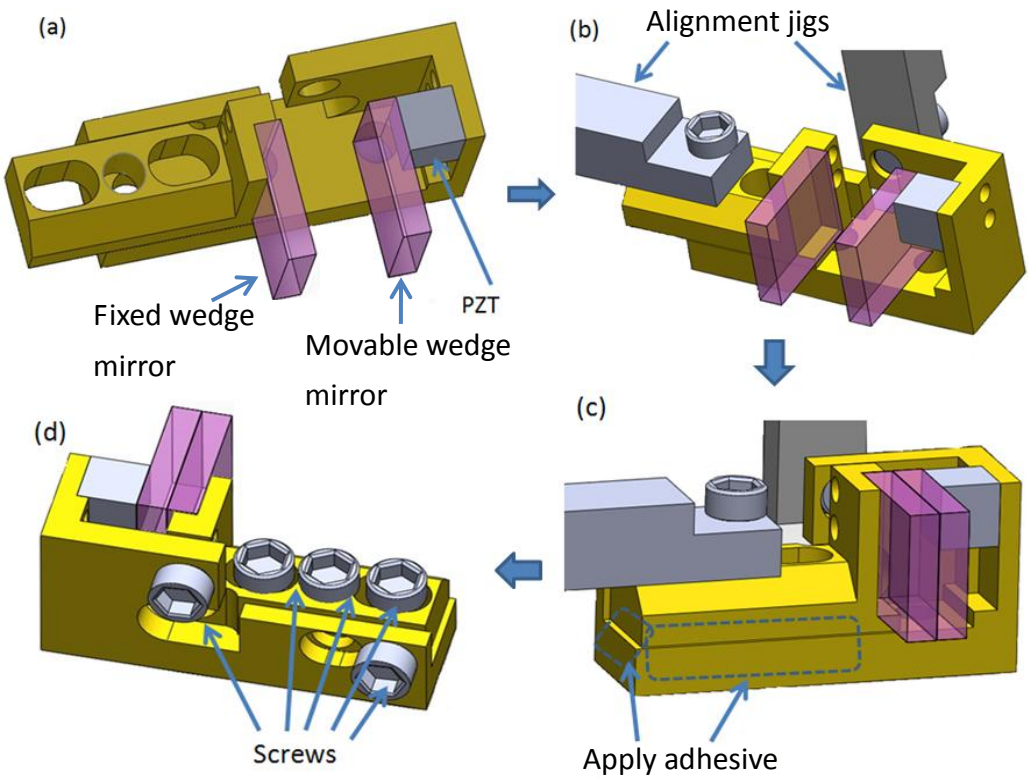

Fig. 3.3 Structural design and fabrication procedures of the tunable filters. (a) Fix the wedge-shaped mirror onto the copper frame and fix the PZT and the other wedge shape mirror onto the L-shaped copper frame; (b) use the alignment jigs to hold and adjust the mirrors to be parallel; (c) add the instant glue to the gap between the two copper frames; (d) release the frames from the alignment jigs and add the screws for fixation and stabilization.

When the tunable filter is adhered by the 415 glue and released from the clamp (Fig. 3.3(d)), the parallelism of two mirrors is usually spoilt. To solve this problem, five screws are used to finely tune the parallelism of two mirrors. After that, small amount of glue is applied onto the screws to secure the contact of screws with the mirrors,

which improves the stability and also strengthens the tunable filter.

In the screw tuning mechanism (see Fig. 3.4), screw (2) acts as the rotation center; screws (1) and (3) are used to tilt the mirror along the Z axis anticlockwise and clockwise, respectively. Moreover, screw (4) and (5) are used to adjust the tilting of the mirror along the Y axis. In this way, the parallelism of mirrors in two rotational directions along the Y and Z axes can be adjusted precisely (see Fig. 3.3). After the tunable filter is assembled, the NOA 61 adhesive is applied to fill the possible space between the screws and screw holes. Therefore, the screws cannot be moved freely and the whole system becomes stable.

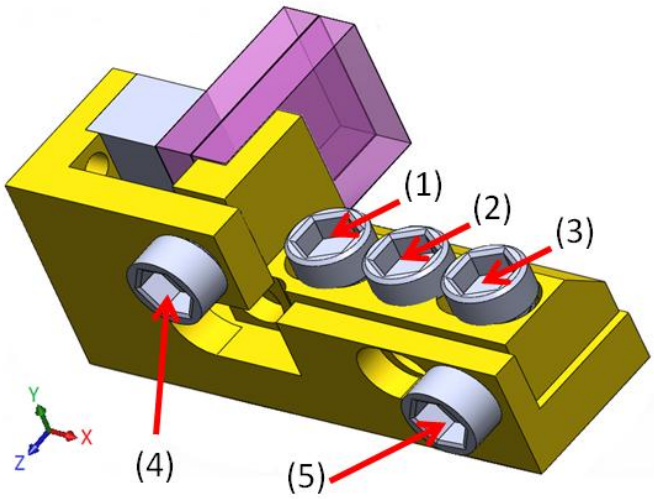

Fig. 3.4 Screws for adjusting the parallelism of mirrors in the tunable filter.

3.4 Precautions

As all parts in the TF rely on the instant glue to assemble, including the PZT, the mirror, the copper frames and the screws, caution should be taken to glue the PZT onto the copper frame and the mirror. If excessive adhesive flows to the sides of PZT, it would restrict the displacement of PZT after the glue is cured. This is one of the critical steps in the assembly of TF and often causes the failure of the whole TF. Therefore, using a toothpick to spread small amount of glue to the one side of PZT, after that, to prevent any glue flows to other sides of PZT, acetone is used to clean it. Moreover, to ensure the size of cavity length is constant at all points, one more PZT actuator can be added. For instance, two PZT actuators, which are attached to two sides of a mirror, can provide an even compressive and extended force to the mirror when a bias is applied on it. Nevertheless, these are only the problems of manual assembly. They can be easily solved when automation machines are used to control the amount and position of glue.

Chapter 4
Experimental Results of Piezoelectric Tunable Filters

This chapter will show the experimental results of the PZT tunable filters, including the tuning property, the peak shifting against bias and the dynamic response of TF. Moreover, some improvements will be elaborated to enhance the performance of PZT-TF. Furthermore, the solution of solving the hysteresis and creeping problems, which are caused by PZT, will be investigated.

4.1 Experimental results

4.1.1 Transmission spectrum and tuning range

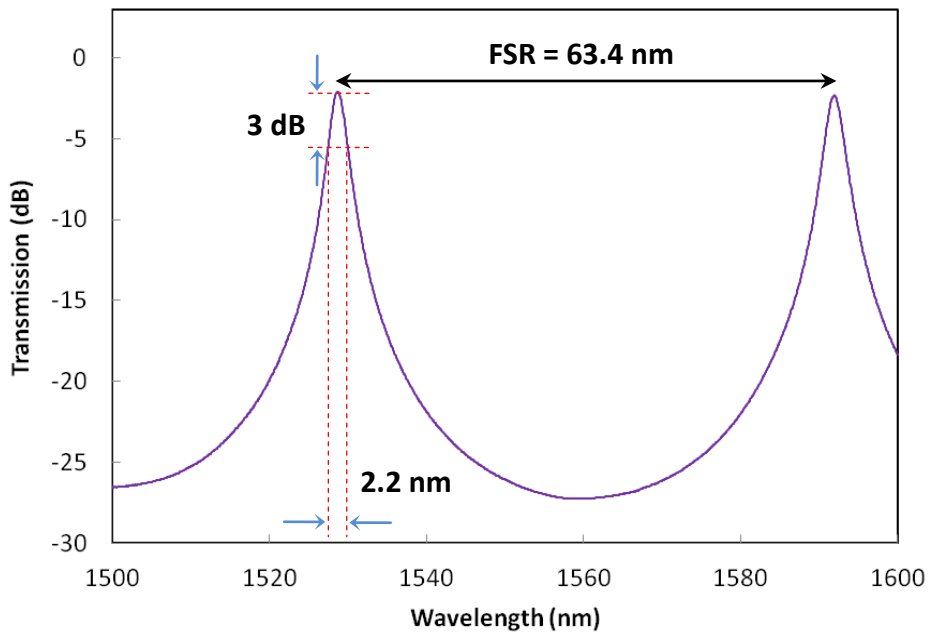

Fig. 4.1 Transmission spectrum of tunable filters.

For the tunable filter using the mirrors R=0.95 and the cavity length L=19 μm, its measured spectrum is shown in Fig. 4.1, and the main specifications are listed in Table 4.1. As seen from Fig. 4.1, the transmission peaks have an FSR of 63.4 nm. The insertion loss is typically about 1 dB, and is only 0.5 dB for the best samples. The contrast between the peak and the bottom is 25.2 dB. At the transmission peaks, the 3-dB linewidth (i.e., FWHM) is 2.2 nm and the 0.5-dB linewidth is 0.7 nm. The finesse is $\frac{64.4}{2.2} = 28.8$. Here the 0.5-dB linewidth is measured because it is an important parameter for side mode suppression in tunable lasers. In the lasers, a difference of 0.5-dB in the roundtrip gain between the peak mode and the second-highest mode is required to obtain a side mode suppression ratio > 30 dB. Therefore, the 0.5-dB linewidth indicates the minimum spacing between the laser peak mode and its side modes.

Table 4.1 Specifications of the piezoelectric tunable filters.

	Designed value	Measured value
FSR	60 nm	63.4 nm
Insertion loss	Ideally, 0 dB	0.5 dB
FWHM (3-dB linewidth)	4.5 nm	2.2 nm
0.5-dB linewidth	1.6 nm	0.7 nm
Finesse	61.2	28.8
Contrast	17.9 dB	25.2 dB

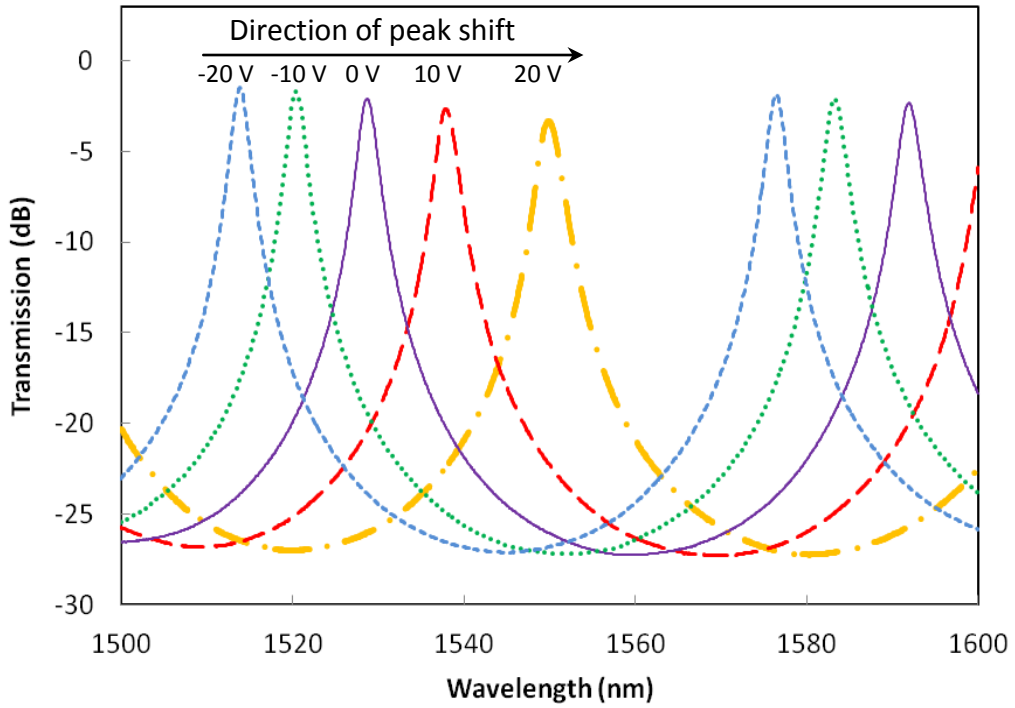

Fig. 4.2 Tuning of the transmission spectrum when the tunable filter is driven by a voltage from – 20 V to + 20 V.

The tuning capability of the filters is also measured. The curves in Fig. 4.2 show the transmission spectra of the tunable filters when subjected to different PZT driving voltages. It can be seen that the transmission peak can be tuned from 1527.90 nm to 1575.90 nm when the voltage is varied from -20 to 20 V. Within a voltage range of 65 V, the tuning range of the filters can cover one FSR (63.4 nm). With higher driving voltage, the maximum tuning range can reach 80 nm. Table 4.2 summaries the tuning specifications of the PZT tunable filters.

Table 4.2 Tuning specifications of the PZT actuated Fabry-Pérot tunable filters.

	Main Specifications
Tuning sensitivity (nm/V)	±1
Tuning range (nm)	80
Tuning speed (ms)	1
Time delay (μs)	5

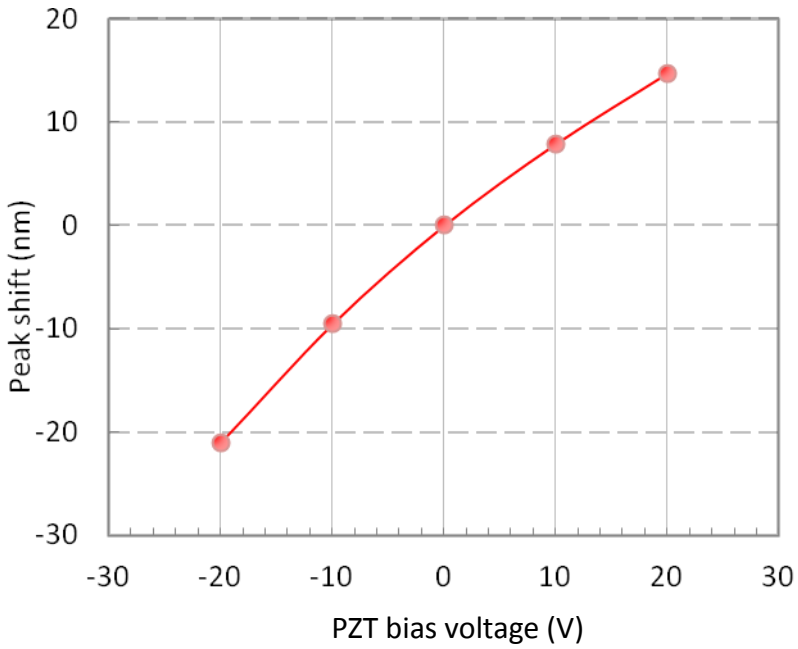

Fig. 4.3 Peak shift of the tunable filters as a function of PZT bias voltage.

The peak shift as a function of the PZT bias voltage is plotted in Fig. 4.3. It shows approximately a linear relationship, with a tuning sensitivity of ±1 nm/V over -20 V to +20 V. It should be noted that the data in Figs. 4.2 and 4.3 are measured when the PZT bias voltage is continuously increased from -20 V to +20 V. Due to the hysteresis and creeping problems of the PZT actuator, the PZT displacement and thus the peak shift

are strongly dependent on the driving history. For example, when the bias is applied from 0 to 20 V and is then returned to 0 V, it does not go back to the original starting point. The charge-drive method can tackle these problems, which will be presented in sub-session 4.3.2.

4.1.2 Dynamic response

The setup for measuring the response speed of the tunable filters is shown in Fig. 4.4. A laser of wavelength 1551.5 nm (near the initial transmission peak) goes through the tunable filter and a generator applies a square wave to drive the PZT actuator (see Fig. 4.4(a)). Then, the transmitted powers for the tunable filters under two levels of bias voltages are indicated by P_1 and P_2 in Fig 4.4(b). The change of the transmitted light is received by a photodetector to convert into electric signals before being displayed by the oscilloscope. Fig. 4.4(b) shows the initial and shifted spectra when the photodetector in Fig. 4.4(a) is replaced by the Oscilloscope Analyzer (OSA). The power oscillation is because the square wave applied to the PZT varies the transmission intensity of light during the wavelength sweeping of OSA. From the response curves, we can see that the settling time of tunable filters is about 1 ms (see Fig. 4.5(a)) and the delay time is about 5 μs (see Fig. 4.5(b)).

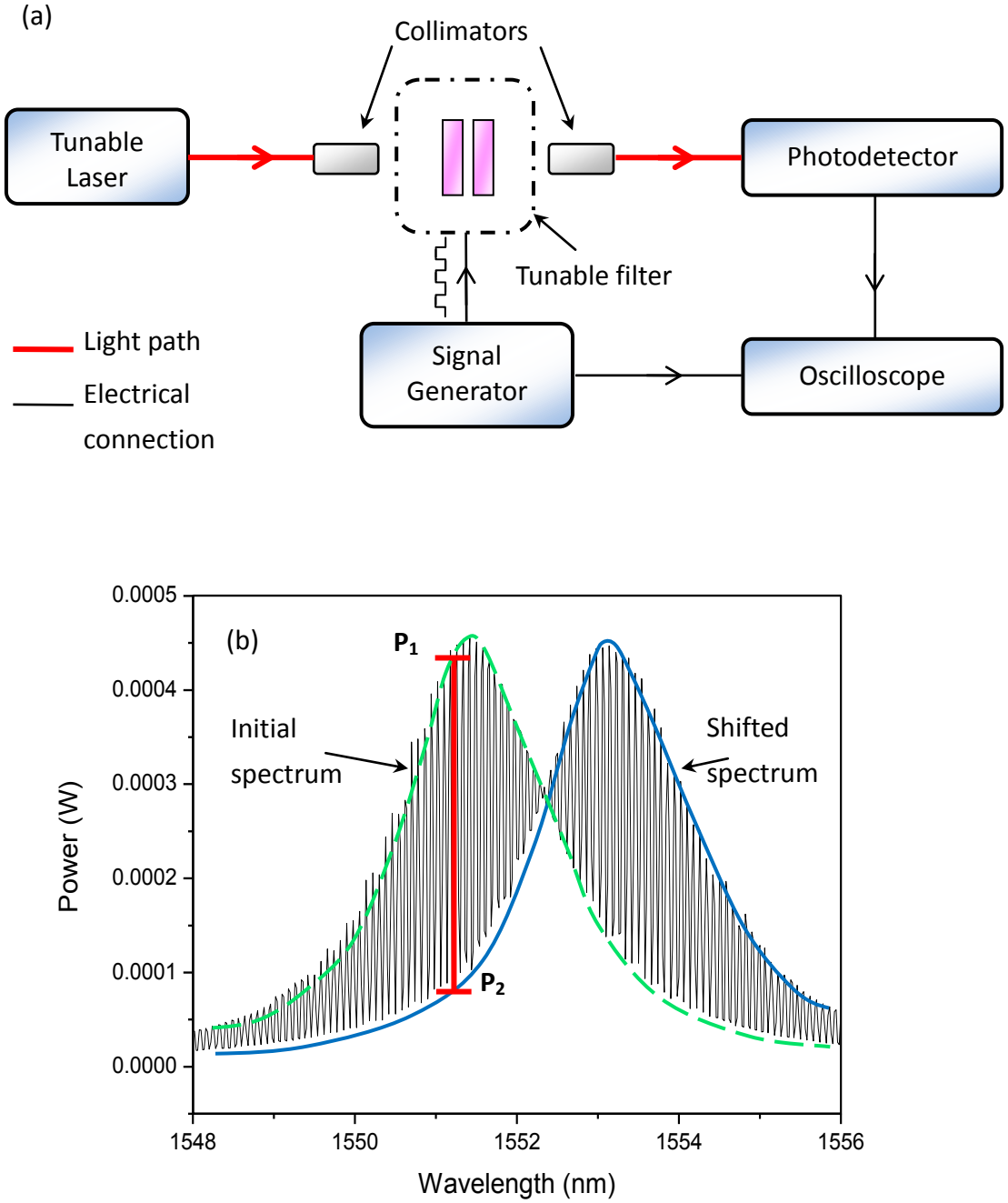

Fig. 4.4 Measurement of the response speed of the tunable filters. (a) Experimental setup; (b) change of transmitted power in response to the PZT bias voltage.

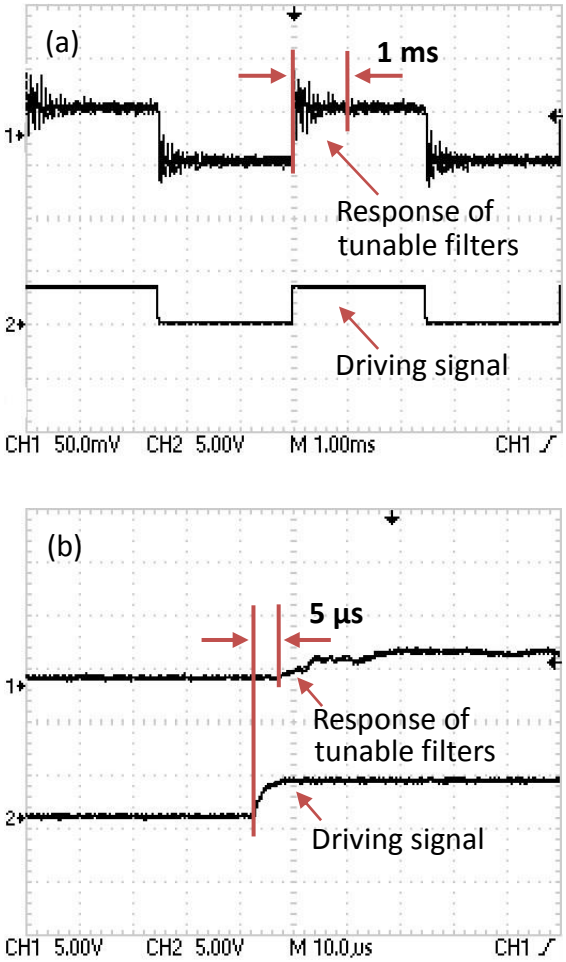

Fig. 4.5 Measurement of the dynamic response of the tunable filters. (a) Settling time; (b) time delay.

4.2 Experimental issues

4.2.1 Monitoring of mirror parallelism

The parallelism of two wedge-shaped mirrors of a tunable filter can be easily determined by the quality of interference fringes. When the bright fringe appears at the middle of the mirror and no more than one fringe is observed over the whole mirror area, its loss is minimized (not larger than 1 dB). Fig. 4.6 shows the interference patterns of

the tunable filters at different states. When the mirror parallelism is deteriorated, more fringes start to appear, and consequently the insertion loss is increased quickly. Table 4.3 lists the losses of different states. Based on this relation, the mirror parallelism can be indicated by the insertion loss rather than the fringe pattern. This simplifies the experiments.

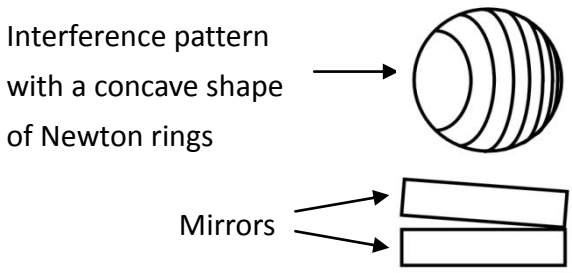

Fig. 4.6 Interference pattern of two non-parallel mirror of PZT-TF.

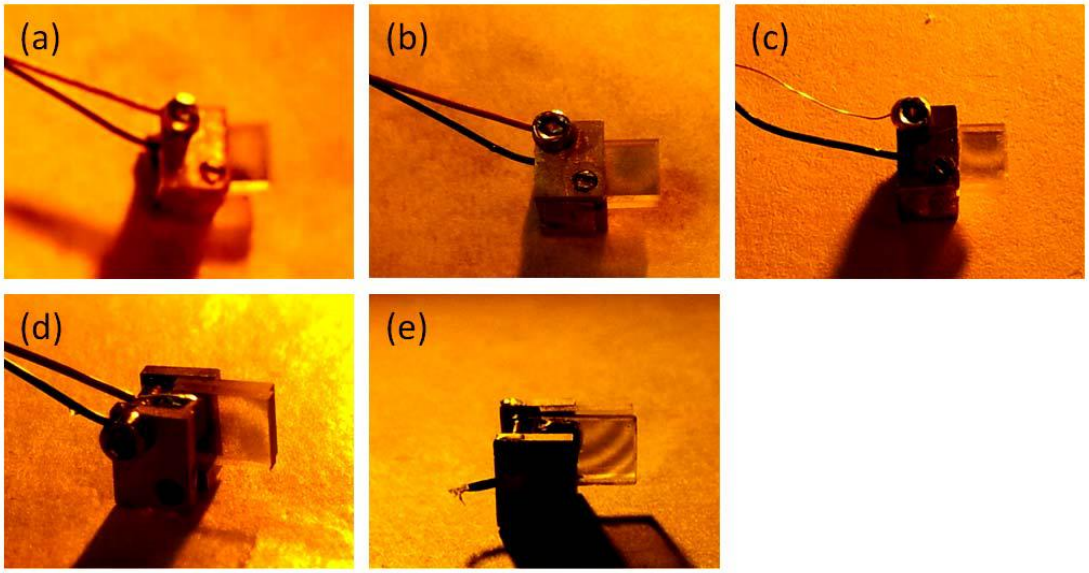

Fig. 4.7 Photos of the interference patterns when the mirror parallelism is deteriorated. (a) Minimal insertion loss when the bright spot is at the center of mirror; (b) central spot and another ring start to appear, the insertion loss is about 1.0 dB; (c) central spot

is shifted upward, the insertion loss reaches 1.4 dB; (d) two dark fringes appear, the insertion loss reaches 1.5 dB; (e) bright spot disappears and dark fringes increase, the insertion loss goes up to 2.5 dB.

Table 4.3 Insertion loss and fringe appearance of the tunable filters.

Tunable filters	Insertion loss (dB)	Fringe appearance
Fig. 4.7(a)	0.8	Bright fringe at the centre
Fig. 4.7(b)	1.0	Centre bright fringe and ring appear
Fig. 4.7(c)	1.4	Centre bright fringe shifts upward
Fig. 4.7(d)	1.5	Two dark fringes appear
Fig. 4.7(e)	2.5	Bright fringe disappears and dark fringes increase

4.2.2 Stability of tunable filters

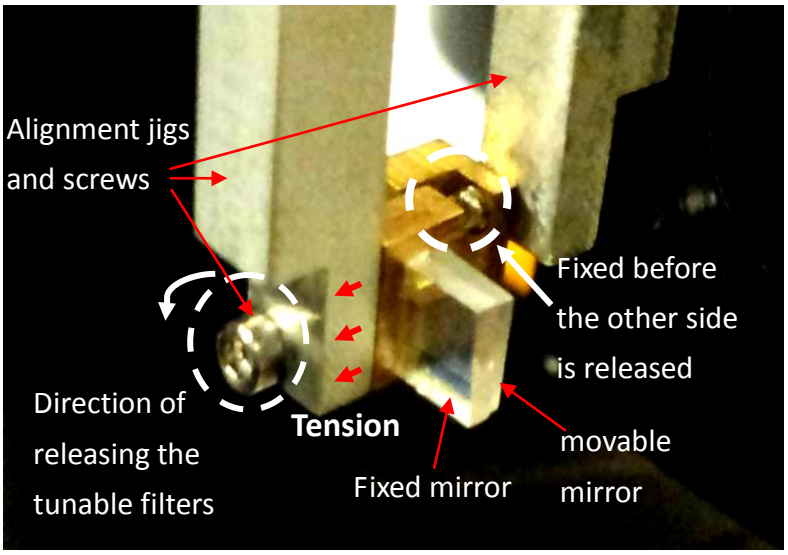

Fig. 4.8 Tension after the tunable filter is released from the alignment jig.

After the adhesive glue was applied to the brass parts of the tunable filters, the loss typically ranges from 0.8 to 1.2 dB while the 0.5-dB linewidth and the 3.0-dB linewidth range from 0.8 to 1.0 nm and 1.9 to 2.5 nm, respectively. The insertion losses would be gradually increased, which might be caused by the following reasons: (1) in the fabrication of tunable filters, the two copper frames are glued together by the instant glue (see Fig. 3.2(c)). Due to the residual stress of the glue after curing, the parallelism is usually degraded. As a result, the insertion loss is increased after the adhesion. (2) Referring to Fig. 4.8, the fixed mirror and the movable mirror are screwed to two alignment jigs separately during the assembly process. After the mirrors are aligned to the best parallelism and are glued together, they are detached from the jigs by releasing the screws. Such release process would affect the mirror parallelism unavoidably. Therefore, great care should be taken during the release process, i.e. release the TF gently from the clamp and make sure the glue is entirely fixed to TF before releasing. To adjust the mirror parallelism, the adjustment screws in the copper frame (see Fig. 3.3) can be used, as described in sub-session 3.2. The increases of insertion loss due to the residual stress and the release process can be offset by using the five alignment screws to fine tune the mirror parallelism after the release.

4.3 Problem and improvement

4.3.1 Structural problems

1st design

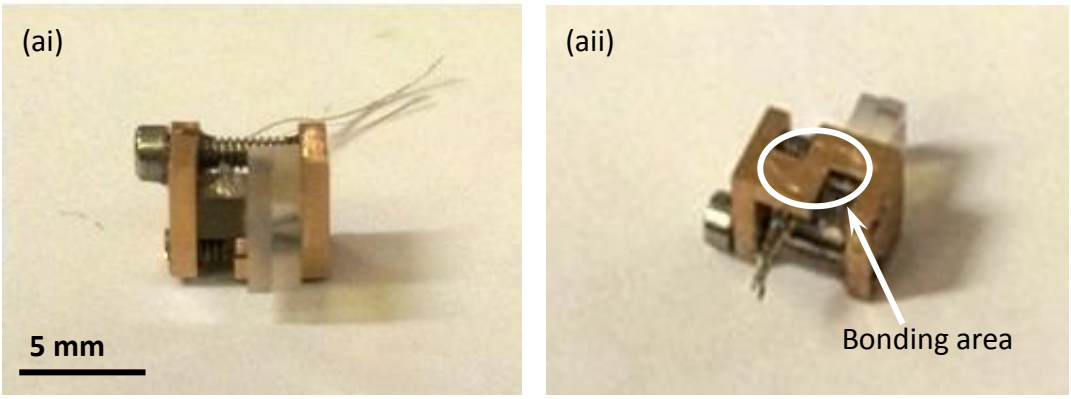

2nd design

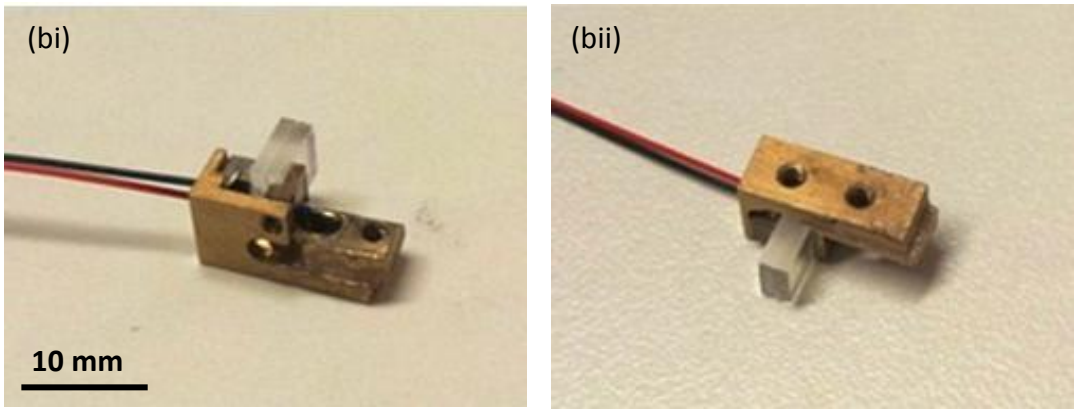

3rd design

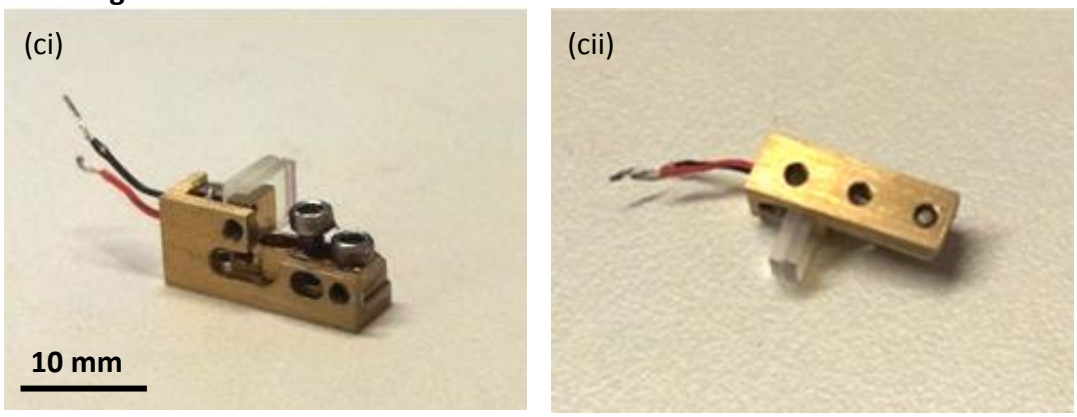

Fig. 4.9 Summary of three designs of tunable filters.

Table 4.4 Power loss of different design tunable filters after one week.

Insertion loss (dB)	**1st design**	**2nd design**	**3rd design**
Initial	0.9	0.9	0.9
Final (After 1 week)	5.0	1.5	**1.05**

In the first part of the research work, three different designs of the tunable filters were designed and fabricated. The photos are shown in Fig. 4.9 and their stabilities as indicated by the change of insertion loss over time are listed in Table 4.4. From Table 4.4, the 1st design has the insertion loss of only 0.9 dB right after the fabrication, but it deteriorates to 5.0 dB after one week of storage. To strengthen the mechanical structure and to enhance the stability, a series of improvements have been adopted, leading to the 2nd and 3rd design. For the 2nd design, the insertion loss is increased to 1.5 dB after one week, while for the 3rd design; it remains almost no change, showing the improvements are really effective. Below describes the details.

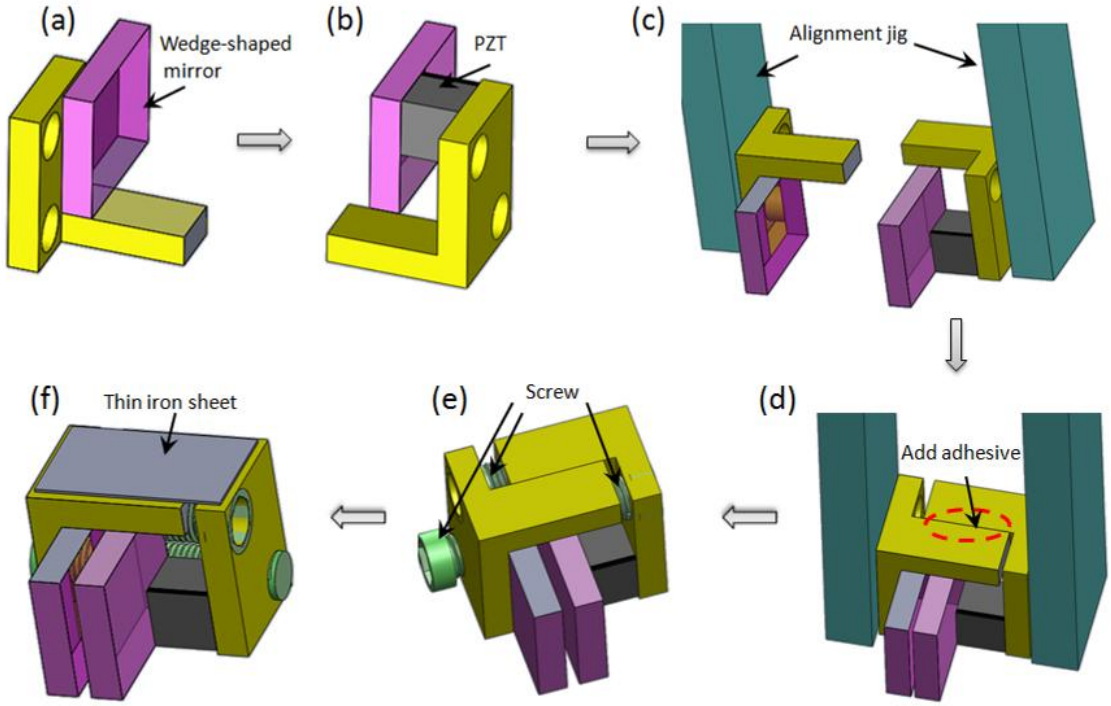

Fig. 4.10 Procedures of fabricating the tunable filters of the 1st design. (a) fix one of the wedge-shaped mirror onto the L-shaped copper frame; (b) fix PZT and another wedge-shaped mirror onto another L-shaped copper frame; (c) use the alignment jig to adjust the mirrors to be parallel; (d) add the 415 glue to the gap between the two L-shaped copper frames; (e) add the screws and use the 415 glue to fix them; (f) fix a thin iron sheet of 0.1-mm thick onto the bottom of the tunable filters.

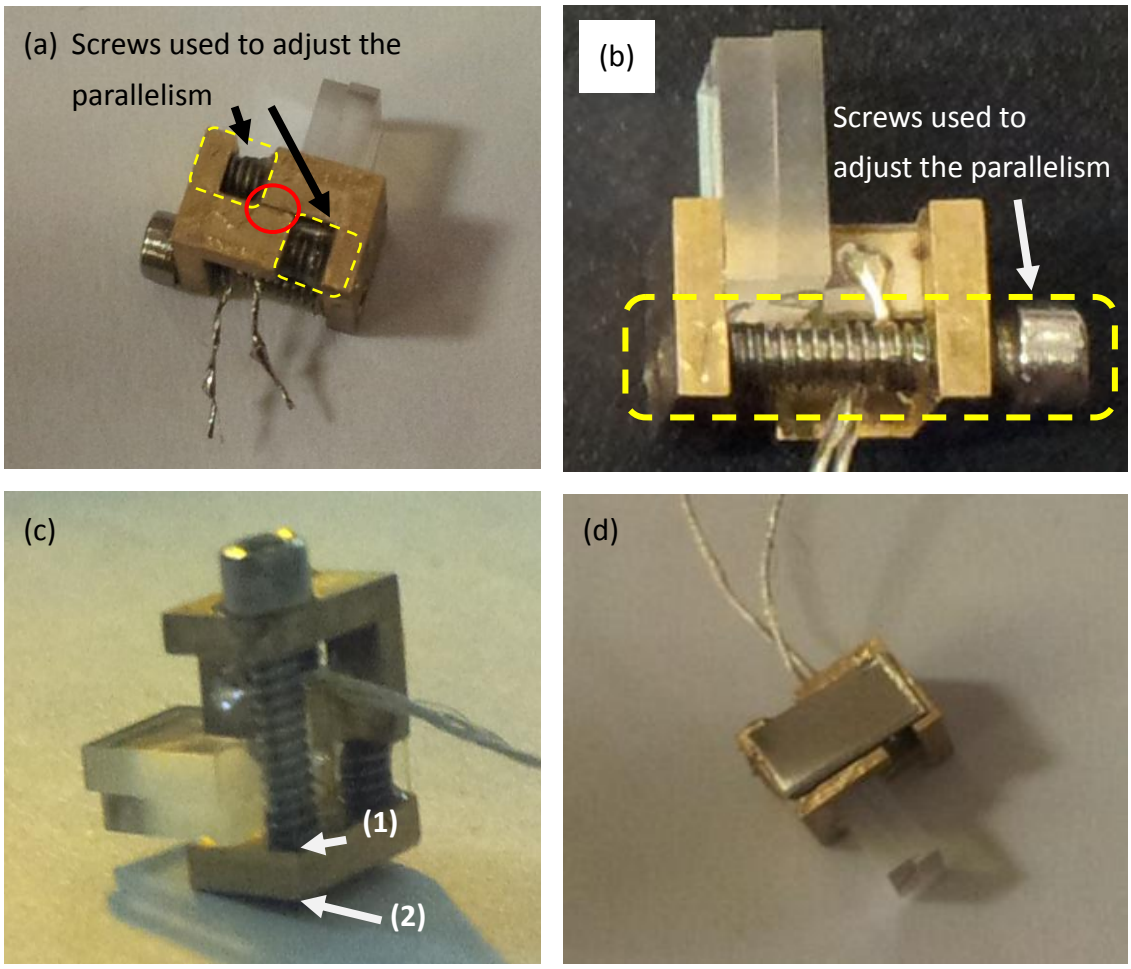

Fig. 4.11 Photos of the 1st design tunable filters. (a) Bottom view; (b) top view; (c) adhesive is added to the position (1) and then diffuses to position (2); (d) gluing a piece of iron thin sheet at the bottom of the tunable filters.

The fabrication of the 1st design tunable filters is shown on Fig. 4.10. As mentioned previously, after the tunable filter is released from the jigs, the parallelism of two mirrors is usually deteriorated. In the 1st design, three screws are used to finely tune the parallelism of two mirrors (see Fig. 4.11). After that, a small amount of glue is applied to the screws themselves to secure the contact of the screws with the mirrors, improving the stability of tunable filters. Finally, a 0.1-mm thick iron sheet is fixed onto

the bottom of the copper frames by the glue for further improving the stability and strengthening the tunable filters.

In the screw tuning mechanism, the upper screw is used to pull the two copper frames whereas the bottom screws are used to push them away in another direction. In this way, parallelism of mirrors in two directions can be adjusted (see Fig. 4.11(a)). After the tunable filter is assembled, the instant adhesive is applied to fill the possible space between the screws and screw holes (see Fig. 4.11(b)). To ensure the gap is fully filled, the adhesive is added at position (1) and it will diffuse to the position (2). In this way, the gap is completely filled up, the screws cannot be moved freely anymore and the whole system becomes more stable (Fig. 4.11(c)).

Apart from it, sticking a piece of thin metal at the bottom of the tunable filters would enhance the stability of the whole system substantially. Although the two L-shaped copper frames are joined using the instant glue (see also Fig. 3.2(c)), the bonding strength is still weak since the bonding region is relatively small. Hence, the assembled tunable filters can be broken up easily during screwing. Once this happens, it is difficult to take out the tunable filter for repair, after it is assembled into the butterfly packaging box of the tunable laser. As the tunable filter is adhered by the same type of instant glue to the butterfly box, debonder has to be used. However, the debonder not only debonds the glue in between the tunable filter and the butterfly box, but also attacks the joining region of two L-shaped copper frames. Gluing a piece of thin metal at the bottom of the tunable filters can largely avoid debonding the joining region of the two copper frames. Moreover, the structure of the whole system is also enhanced due to the much enlarged contact area between the thin metal sheet and the bottom of the

tunable filter. With the thin metal, two copper frames of the tunable filter cannot be separated easily (see Fig. 4.11(d)).

Although the 1st design tunable filters can be fabricated easily, it breaks easily and cannot stand long. As mentioned before, a thin metal is fixed at the bottom of the TF; however, the loss still increases after one week. It might be attributed to the stress between the small bonding area and the large thin metal, which cannot be tuned by the screws anymore as the bonding region is fixed. Hence, the assembled tunable filters still deteriorates but in a much slower rate. As the stability of the 1st design tunable filters is very low and the insertion loss increases significantly after one week, it cannot be used in any devices or systems. Therefore, the 2nd design tunable filter is made.

The 2nd design is stronger than the first design tunable filter since a large copper base is fabricated instead of bonding two small frames together, and the parallelism of the mirrors can be adjusted by screw tuning. However, creeping can still happen between two copper frames (Fig. 4.9(b)). Although some screws are added to fix the two copper frames, the entire filters cannot be fixed firmly. The stress of the glue causes the creeping on two sides of TF. This gradually deteriorates the parallelism of mirrors. Therefore, after one week, the insertion loss of the tunable filter is increased from 1.13 dB to 1.5 dB.

Although the 2nd design is quite stable, it is still not good enough. Hence, the 3rd design tunable filter is developed. By adding a lateral copper board to the base of the tunable filters, it could prevent any large lateral creeping (Fig. 4.9(c), see also Fig. 3.3). Moreover, the number of screws holes is increased to insert more tuning screws. After the TF is released from the jigs, the tuning screws can compensate the change of mirror

parallelism (see Fig. 3.3). As a result, this tunable filter yields a small insertion loss, and a high stability.

4.3.2 Hysteresis and creeping of piezoelectric actuator

4.3.2.1 Driving methods of PZT

The PZT driving can be classified into two categories: open-loop operation and closed-loop operation. In the open-loop operation, there are basically three driving methods: *voltage drive method*, *capacitor insertion method* and *charge drive method*.

The simplest method is to directly apply a voltage to the terminals of PZT. This is the *voltage drive method*. Due to the well-known hysteresis and creeping behavior, the PZT displacement corresponds roughly to the applied voltage but varies over a range of typically 25% of the displacement (see Fig. 4.12). High position accuracy and one-to-one relationship between the displacement and the voltage remain a challenge to the voltage drive method.

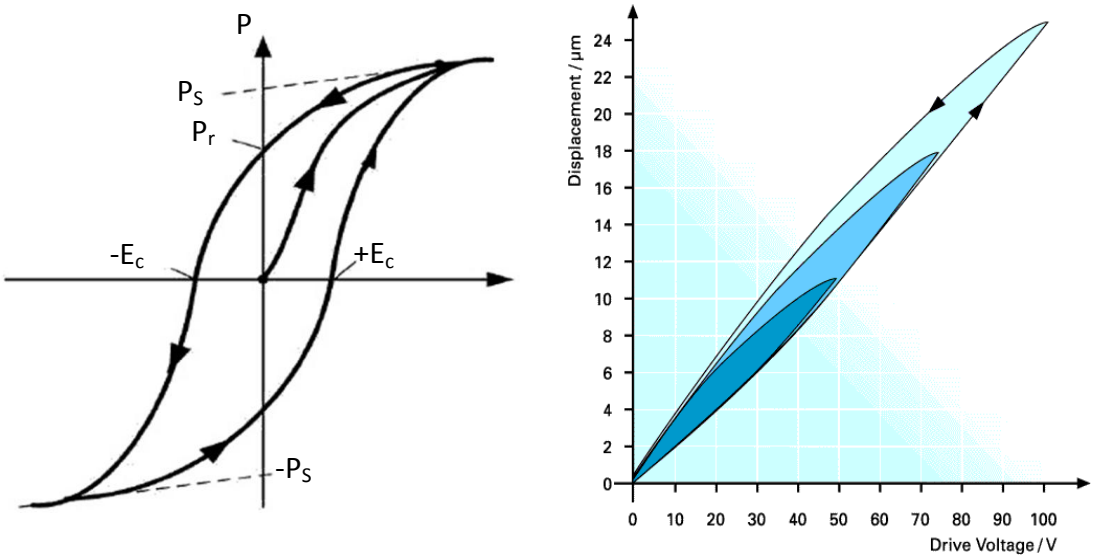

Fig. 4.12 Hysteresis curve of PZT under voltage drive.

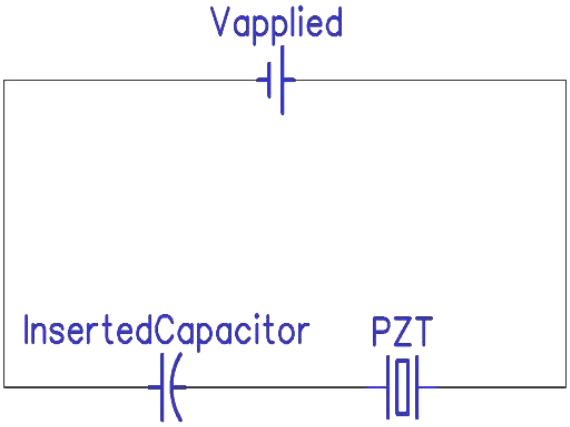

Fig. 4.13 Circuit diagram for capacitor insertion method.

In order to reduce the influence of hysteresis and creeping, an improved method called the *capacitor insertion method* can be used. As shown in Fig. 4.13, a capacitor is inserted in series with the PZT, and the applied voltage is divided between the inserted capacitor and the PZT. The PZT characteristics become more linear with smaller capacitor. However, only a small proportion of the applied voltage is applied to the PZT, reducing the PZT displacement. To get the same amount of displacement, a much higher voltage is needed as compared to the voltage drive method. This is the reason why this method is not commonly used.

The *charge drive method* provides another efficient approach to reduce the hysteresis and creeping. In the *voltage drive method*, the PZT behaves like a non-linear capacitor. The value of its capacitance varies even when the applied voltage is kept constant. As a result, the charge stored in the PZT is changed as well. It is the main reason of the nonlinear hysteresis and the creeping behavior. To compensate the capacitor change, the charge input to the PZT is controlled and monitored. This leads to a significant reduction of hysteresis and creeping.

4.3.2.2 Charge drive method

As the charge drive method needs to monitor the amount of charges, it requires a closed-loop operation. The whole circuit diagram of charge drive is shown in Fig. 4.14. A high-input-impedance operational amplifier and a stable sensing capacitor C_r are used to construct an integrator (see Fig. 4.14(b)). The capacitance of the sensing capacitor is chosen based on the maximum charge load of the PZT and the saturated output voltage of the integrator. The switch K in the circuit is for discharging. This is to ensure that the PZT and the sensing capacitor are completely discharged when no voltage is applied. When a voltage V_p is applied to the PZT, some charges flows in. As the input impendence of operational amplifier is very high, no current can flow into the input of operational amplifier. Therefore, the charges stored in the PZT are the same as those in the sensing capacitor. By monitoring the voltage output V_q, the charge of PZT can be calculated.

$$\text{Charge stored} = C_r V_q \tag{4.1}$$

To supply enough charges to the PZT, a high voltage V_p is needed. Fig. 4.14(a) shows the circuit diagram of a voltage amplifier. By choosing suitable resistance values of R_1 and R_2, different voltage gains can be obtained.

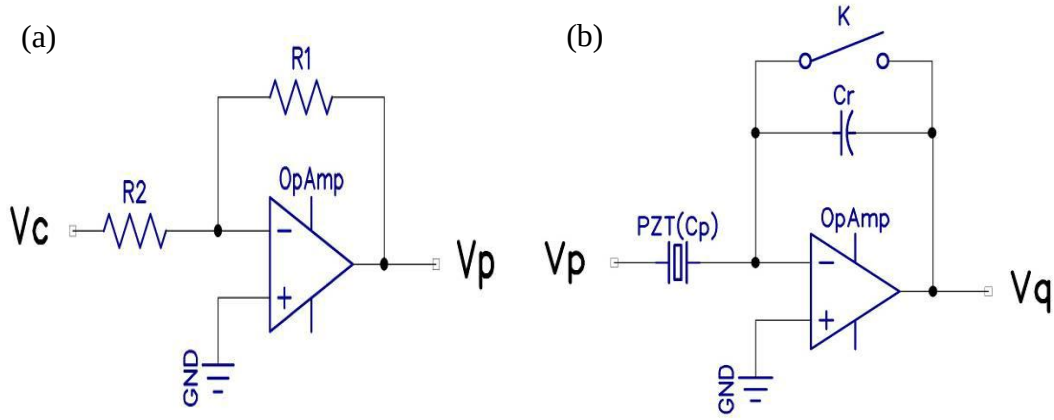

Fig. 4.14 Circuit diagrams of the charge drive method. (a) Voltage amplifier; and (b) integrator.

Table 4.5 Parameters of electrical components used to construct the circuit for the charge drive method.

R_1	R_2	C_r	C_p
40 kΩ	20 kΩ	0.1 μF	0.022 μF

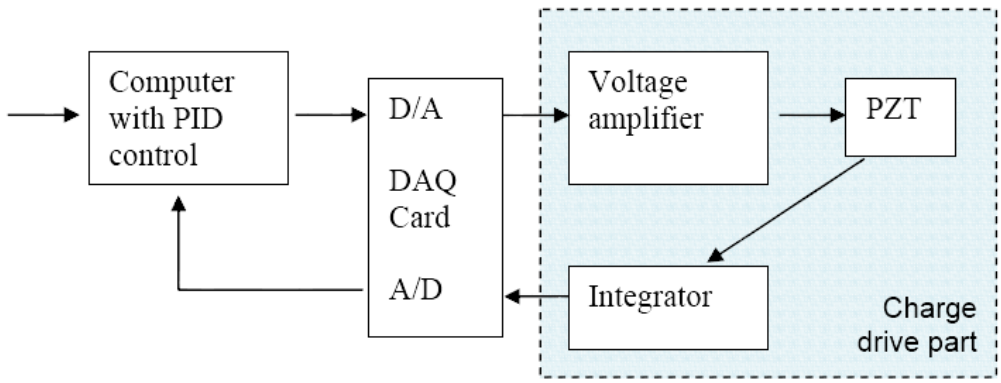

Fig. 4.15 PID feedback control for charge drive based on the charge feedback.

The closed-loop feedback control system for charge drive is shown in Fig. 4.15. First, a set point is given to the computer that is running the PID control software. It gives a signal to the data acquisition card (DAQ), which processes the digital-to-analog (D/A) conversion. The voltage signal is amplified by the voltage amplifier and used to drive the PZT. Then, the charge feedback signal is obtained from the voltage output of the integrator and is converted into the digital signal, which is transmitted to the computer. The PID control software adjusts the voltage signal and repeats the whole procedures until the set point is reached.

The experimental results of the PZT displacement as a function of the charge set point (i.e., the amount of charges) are plotted in Fig. 4.16. The graph shows a good linearity between the PZT displacement and the set point (i.e., the amount of charges). More importantly, the graph shows a one-to-one relationship between the PZT displacement and the set point. In addition, the graph reproduces itself nicely over a long run of sweeping. As a result, the hysteresis and creeping problem is circumvented. The charge drive is essential for the operation of tunable filters and thus the further realization of the tunable lasers. Without which, PZT actuators cannot be used in the butterfly packaging. This is because the PZT has to be very small (2 mm$\times$2 mm$\times$2 mm) and cannot use strain gauges for displacement monitoring.

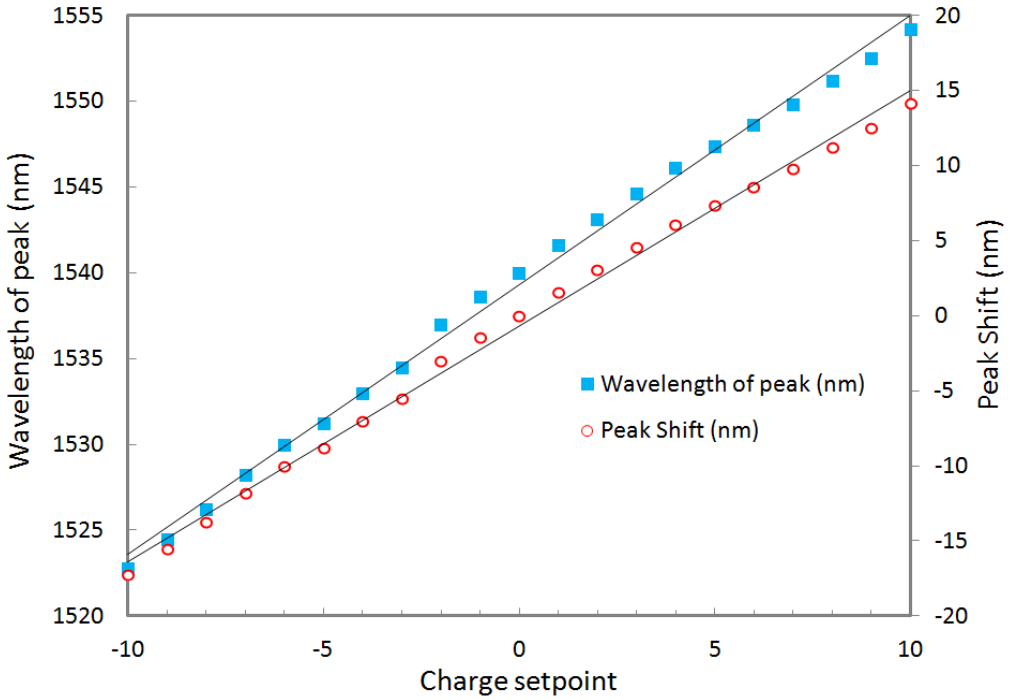

Fig. 4.16 Measured PZT displacement as a function of the charge using charge drive feedback control.

4.4 Application of PZT tunable filters in tunable lasers

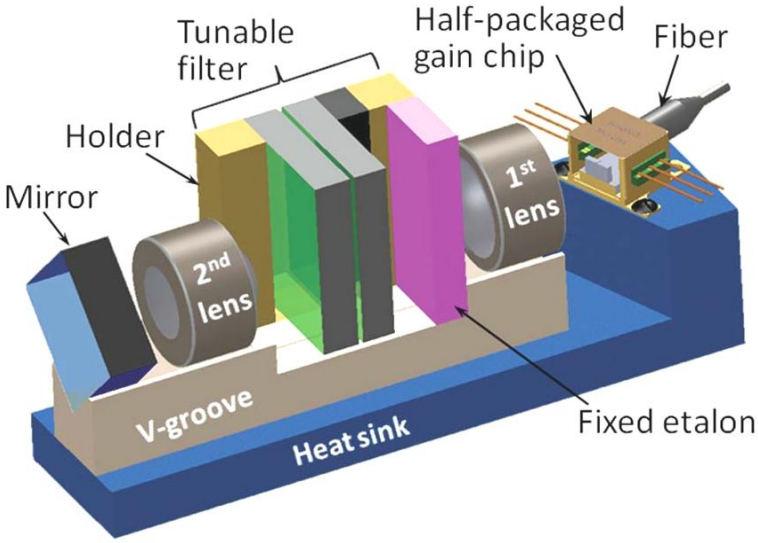

Fig. 4.17 3D structural diagram of the narrow-linewidth external-cavity tunable laser that utilizes the PZT-tunable filter for wavelength tuning.

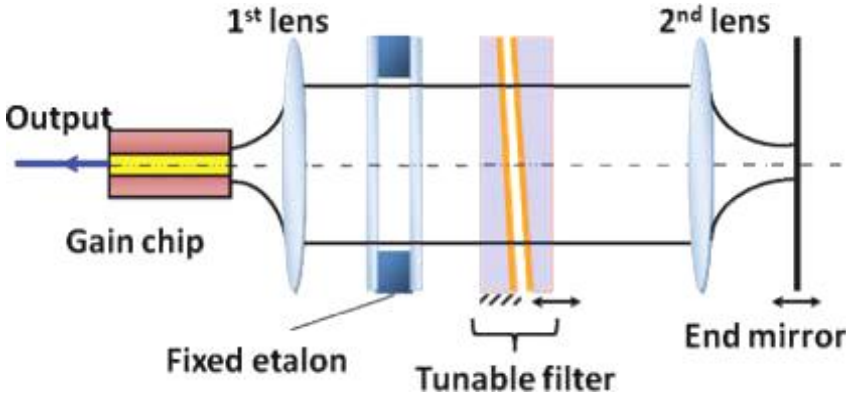

Fig. 4.18 Optical design of the narrow-linewidth tunable filter. It uses two converging lenses, a fixed etalon and a tunable filter in a retro-reflective configuration.

The PZT-TF has been successfully used in the narrow-linewidth external-cavity tunable lasers. Fig. 4.17 shows the 3D structure of the tunable laser and Fig. 4.18 shows the optical design. As shown in Fig. 4.17, a half-packaged fiber-pigtailed gain chip provides the optical gain. The laser is collimated by the 1st lens before going through the tunable filter (see Fig. 4.18). Then it is focused by the 2nd lens and reflected by an end mirror. The total resonant cavity is between the HR facet of gain chip (i.e., the output side) and the mirror. Wavelength selection in the tunable laser is dependent on three factors: the fixed etalon, the PZT tunable filter and the total resonant cavity (see Fig. 4.19). The fixed etalon defines the standard grid of wavelengths (spaced by 50 or 100 GHz) used in the DWDM systems. It is not tunable. The total cavity provides a dense transmission peaks (due to its long cavity length and thus a narrow mode spacing), which is a side effect. It affects the transmission efficiency (e.g., between 0.6-1.0 in Fig. 4.19) but does not tune the wavelength. In this system, the tunable filter is the only one for wavelength tuning. For example, in the state shown in Fig. 4.19, the target wavelength is $\Delta v = 0$, at which all peaks are met simultaneously. This is the optimal

state, the side mode at $\Delta\nu$ = 50 GHz ($\Delta\lambda$ = 0.4 nm) is suppressed by -0.92 dB by the tunable filter's transmission spectrum, and by -2.3 dB by the total cavity. Altogether, the side mode has a transmission 3.2 dB lower than the peak mode. This introduced a big difference of the gains of the peak mode and the side mode, and eventually leads to > 50 dB difference in the output powers of the two modes. That is, the side mode suppression ratio (SMSR) is expected to be > 50dB, which is very good for a single-wavelength laser. The tuning of wavelength (e.g., to the next mode at 50 GHz) is obtained by shifting the peak of tunable filters, the end mirror is slightly displaced to align all the peaks at $\Delta\nu$ = 50 GHz.

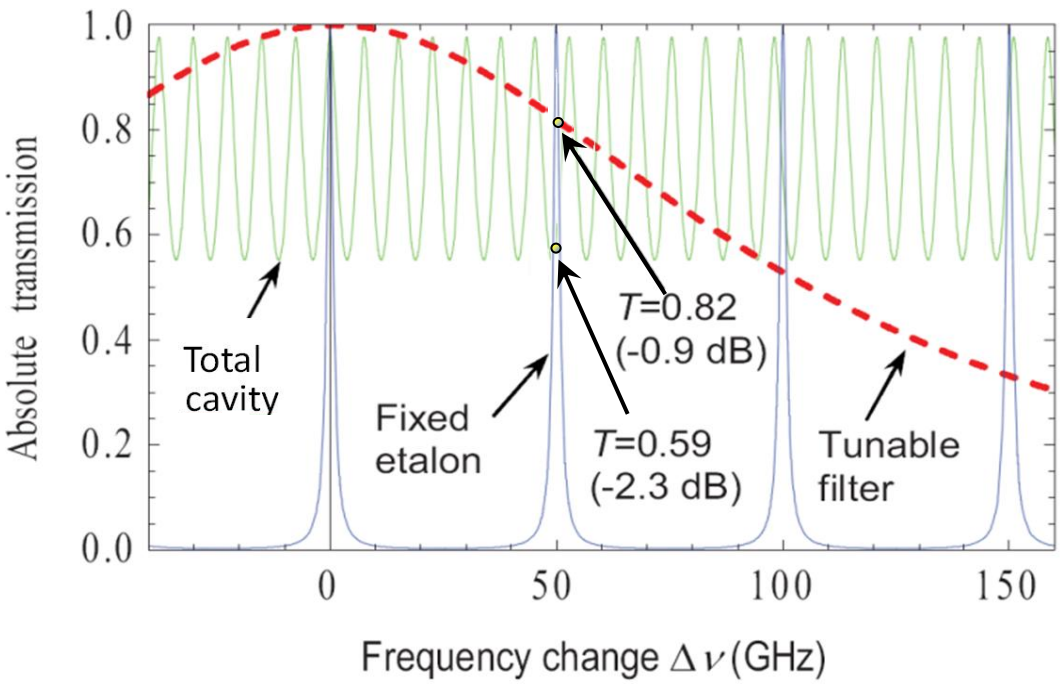

Fig. 4.19 Principle of wavelength selection and tuning in the narrow-linewidth tunable laser.

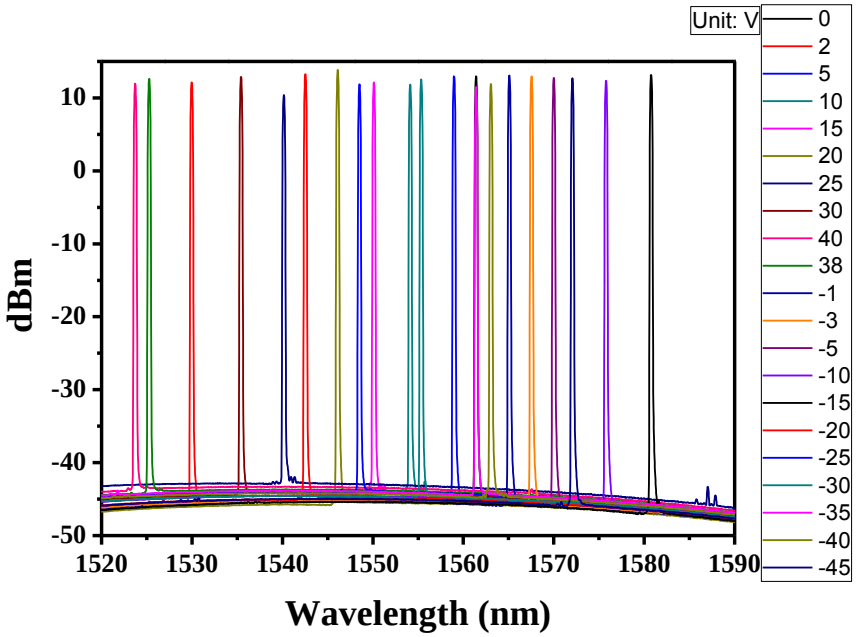

Fig. 4.20 Measured laser output wavelength spectra as tuned by applying different bias voltages to the PZT actuator of the tunable filters.

The experimental result of wavelength tuning of the tunable laser is shown in Fig. 4.20. When the bias voltage is changed from -15 V to 40 V, the laser output wavelength varies between 1523-1581 nm, large enough to cover the C-band (1530-1565 nm) used for DWDM networks.

The output power reaches 12 dBm (16 mW), with an SMSR > 58 dBm. The output linewidth is typically below 20 kHz [23] (not shown in Fig. 4.20), superior to most of the available products (typically > 100 kHz). This shows the PZT tunable filters work well for the tunable lasers.

4.5 Summary

The PZT tunable filters have been successfully developed to achieve large tuning range (> 60 nm), narrow-linewidth (FWHM 2.2 nm), low insertion loss (0.5 dB), fast tuning speed of (1 ms) and polarization independence. In addition, the hysteresis problem of the PZT actuator is solved by using the charge drive method. It has obtained a linear relationship between the PZT displacement (and thus the shift of peak wavelength) and the charge set point. The PZT tunable filters have been successfully incorporated into the narrow-linewidth tunable lasers (see Fig. 4.21) and have obtained very good tunability and laser performance (tuning range > 60 nm, output power 16 mW, SMSR > 58 dB, linewidth < 20 kHz).

This chapter and the previous one constitute the first part of my research work. In the next chapter, the second part of my research work will be presented. It studies a new tuning method for the tunable filters.

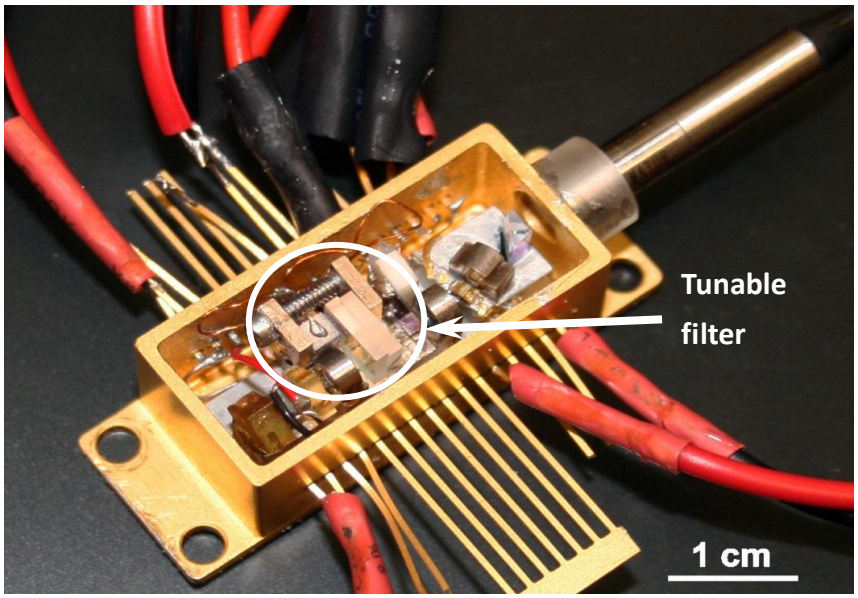

Fig. 4.21 The photo of the butterfly packaged narrow-linewidth tunable laser.

Chapter 5

Design and Fabrication of Electrolyte-Capacitor Tunable Filters

This is the second part of the research work, in this chapter, the working mechanism of the electrolyte-capacitor tunable filter will be discussed and the procedures of fabrication will be described. Additionally, two theoretical models of ECTF, the simple model and the field model, will be elaborated to analyze with the experimental results.

5.1 Working principle of electrolyte-capacitor tunable filters

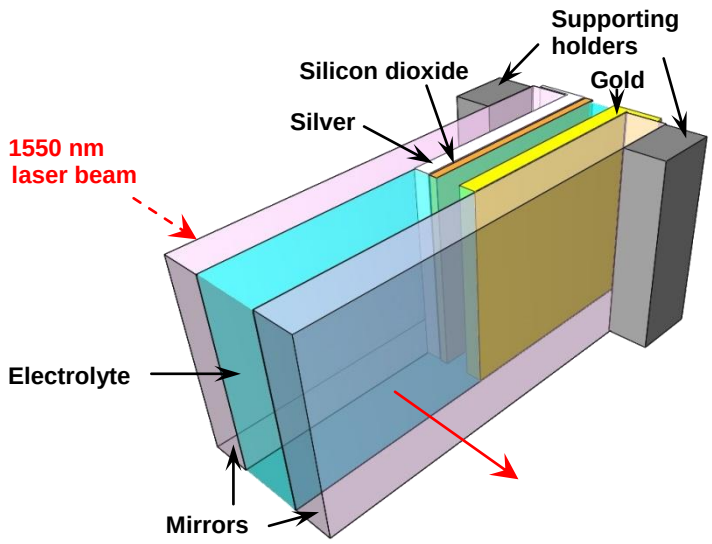

Fig. 5.1 3D structure of the Tunable Filters.

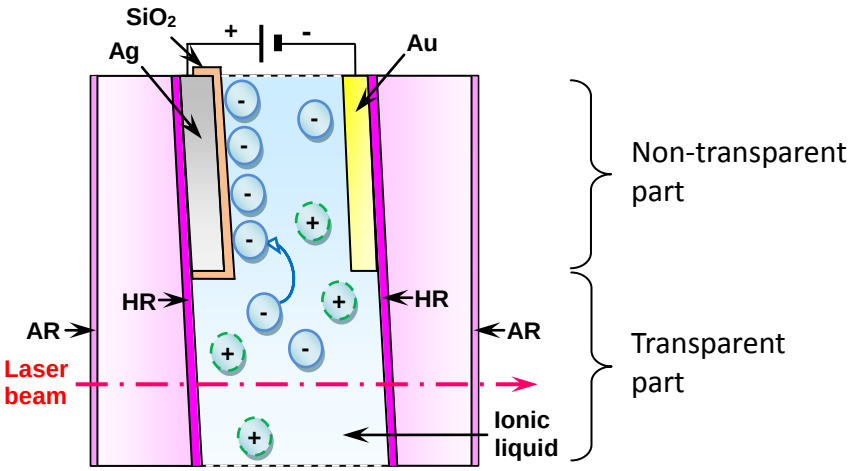

Fig. 5.2 Working principle of the electrolyte-capacitor tunable filters.

The 3D schematic diagram in Fig. 5.1 presents the structure of the electrolyte-capacitor tunable filter, which is composed by a pair of wedge-shaped mirrors. The structure of this ECTF is similar to the PZT actuated tunable filter described in the previous chapter. The working principle is illustrated in Fig. 5.2. In the FP etalon, the non-transparent part is used for tuning whereas the transparent part is used for light propagation and for obtaining the transmission spectrum. A dielectric silicon dioxide thin film is deposited on the silver electrode to provide a high capacitance for charge storage. When a small bias is applied to the electrodes, ions are attracted to move towards the electrodes. Therefore, the ion concentration at the transparent part decreases and the refractive index at that part is varied. When a light beam passes through the transparent part, the peak wavelength is shifted. However, when the bias voltage is removed, the internal electric field will disappear and the ions would diffuse back to return to the state of uniform distribution in the FP cavity again.

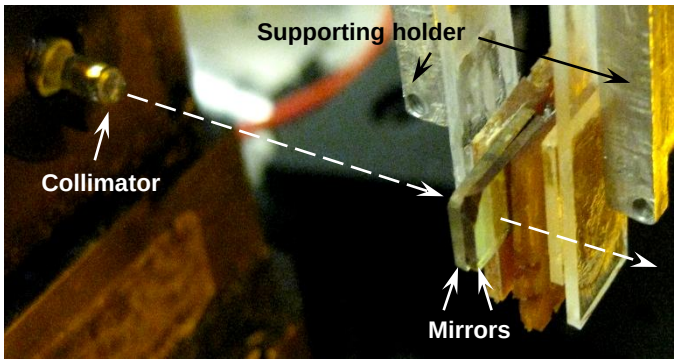

Fig. 5.3 Setup for measuring the tuning performance of tunable filters.

The experimental setup is shown in Fig. 5.3. Both mirrors were put together with 5-axis stage with their coated parts facing each other. A tunable laser beam was coupled using a pair of collimators. The front collimator was used to collimate the entire light beam before entering the tunable filter and the back collimator was used to receive the laser beam. In order to align the two mirrors to be parallel, the best way is to observe the interference patterns to determine the parallelism of mirrors. We used a sodium lamp as a monochromatic light source for illumination. When two mirrors were in parallel, only one Newton ring appeared, indicating that deduced that the insertion loss of TF was the smallest (see Fig. 4.7(a)).

5.2 Theoretical modelling of ECTF

In the electrolyte-capacitor tunable optical filters, a bias voltage applied to the capacitor would attract ions to the capacitor surface, and thus the ion concentration in the FP cavity would be changed. This would in turn vary the refractive index in the FP cavity. In the following parts, two models will be studied: a simple model and a field model. The simple model assumes a uniform change of refractive index and provides a quick estimation. The field model will consider the non-uniform distribution. However,

the results of the field model will show that the non-uniformity is very little in the region of interest (i.e., the region through which the laser beam passes). This shows that the simple model is feasible.

5.2.1 Simple model of ECTF

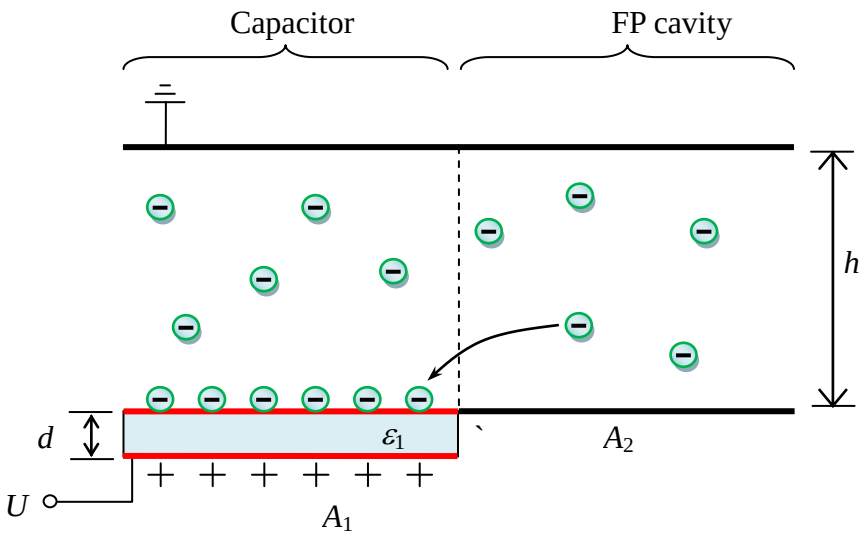

Fig. 5.4 Simple model of the concentration change of ions.

In the electrolyte-capacitor tunable optical filter, the structure can be divided into two regions: capacitor and FP cavity (see Fig. 5.4). The former corresponds to the non-transparent part in Fig. 5.2 and is for applying the bias voltage; whereas the latter corresponds to the transparent part in Fig. 5.2 and is for transmitting the laser beam. As discussed above, the ion concentration and thus the refractive index are dependent on the bias voltage applied to the capacitor (see Fig. 5.4). For a simple estimation, some assumptions are made:

(1) The concentration change of only the negative ion is considered. This is because the abundance of the positive ions is equivalent to the lack of negative ions. With these, it is assumed that the positive ions act as the background and are distributed uniformly. Similarly, we can consider only the positive ions and treat the negative ions as the uniformly-distributed background. The result should be the similar.

(2) The distribution of negative ions in the FP cavity is uniform. Close to the boundary of the capacitor and the FP cavity, there may be some deviation; but away from the boundary, the ions should be distributed almost uniformly.

5.2.1.1 Change of ion concentration

The capacitance of the capacitor

$$C = \frac{\varepsilon\varepsilon_0 A_1}{d} \tag{5.1}$$

here ε is the relative permittivity of film (here SiO_2), ε_0 is the permittivity of vacuum (= 8.854×10^{-12} F/m), A_1 the area of capacitor region, and d the film thickness of capacitor (see Fig. 5.4).

Charges on the capacitor surface

$$Q = CU = \frac{\varepsilon\varepsilon_0 A_1}{d} U \tag{5.2}$$

here U is the bias voltage applied across the capacitor.

Number of negative ions attracted to the top surface of capacitor

$$N = \frac{Q}{e} = \frac{\varepsilon\varepsilon_0 A_1}{ed} U \tag{5.3}$$

here e is the electron charge (= 1.602×10^{-19} C).

Change of number concentration of the negative ions in the FP cavity region

$$\Delta c_N = \frac{N}{V} = \frac{N}{A_2 h} = \frac{\varepsilon\varepsilon_0 A_1}{edhA_2} U \tag{5.4}$$

here A_2 is the area of FP cavity region.

Change of molar concentration of the negative ions in the FP cavity region

$$\Delta c_M = \frac{\Delta M}{V} = \frac{(N/N_A)}{A_2 h} = \frac{\varepsilon_0 A_1}{eN_A dhA_2} U \tag{5.5}$$

here N_A is the Avogadro's number ($N_A = 6.022\times10^{23}$ mol^{-1}).

5.2.1.2 Estimation of using the data of the refractive index of BMIM-PF$_6$

Table 5.1 lists the change of refractive index of BMIM-PF$_6$ in ethanol which are extracted from table 2 of Ref. [37]. In the Table 5.1, x is the molar fraction of BMIM-PF$_6$. It can be converted into the molar concentration c by the expression [39]

$$c = \frac{x\rho}{xM_{IL} + (1-x)M_{ethanol}} \tag{5.6}$$

here $M_{ethanol}$ = 46.07 g/mol.

Using Eq. (5.6) to convert the molar fraction into the molar concentration, we can plot the data of Ref. [37] as shown in Fig. 5.5. Based on the linear fitting, it has

$$n = 0.0129c + 1.3477 \quad (c \text{ in the unit of mol/L}) \tag{5.7}$$

Considering only the concentration of negative ion PF$_6^-$ is changed, we can get

$$\begin{aligned}\Delta n &= \frac{M_{\mathrm{PF6}}}{M_{\mathrm{IL}}} \times 0.0129 \times 1000 \Delta c_M \\ &= \frac{144.96}{284.18} \times 12.9 \Delta c_M \\ &= 6.58 \Delta c_M \quad (\Delta c_M \text{ in the unit of mol/m}^3)\end{aligned} \tag{5.8}$$

here 1000 is for the unit change from mol/L to mol/m^3.

According to the expression of Δc_M in Eq. (5.4), assume $A_1 = A_2$, it has

$$\begin{aligned}\Delta c_M &= \frac{\varepsilon_0 A_1}{eN_A dhA_2} U = \frac{\varepsilon_0}{eN_A dh} U \\ &= \frac{3.9 \times (8.85\times10^{-12})}{(1.602\times10^{-19}) \times (6.022\times10^{23}) \times (150\times10^{-9}) \times (91\times10^{-6})} U \\ &= 2.62\times10^{-5} U\end{aligned} \tag{5.9}$$

here U is in the unit of volt, and Δc_M is in mol/m^3.

Substitute Eq. (5.9) into Eq. (5.8), it gives

$$\Delta n = 6.58\Delta c_M = 6.58\times 1.40\times 10^{-4}U = 1.72\times 10^{-4}U \tag{5.10}$$

Similarly, we can estimate the phase change in the FP cavity, which is expressed as

$$\begin{aligned}\Delta\phi &= \frac{2\pi}{\lambda}\Delta OPL = \frac{2\pi}{\lambda}(2h\Delta n) = \frac{4\times 3.142}{1.55\times 10^{-6}}\times\left(91\times 10^{-6}\right)\times\left(1.72\times 10^{-4}U\right)\\ &= 0.127U\end{aligned} \tag{5.11}$$

here $\Delta\phi$ is in the unit of radian, U in volt.

If the phase change is required to be 2π (equivalently, the peak is shifted by one free spectral range), the required voltage is

$$U_{2\pi} = \frac{2\pi}{0.127} = 49.5\,\text{V} \tag{5.12}$$

The peak shift of $\Delta\lambda$ of FP transmission spectrum can be expressed as

$$\begin{aligned}\Delta\lambda &= \frac{\Delta n}{n_0}\lambda_0 = \frac{1.72\times 10^{-4}U}{1.41069}\times 1550\\ &= 0.19U(nm)\end{aligned} \tag{5.13}$$

here n_0 is the refractive index of BMIM-PF_6 (see Table 5.1), λ_0 is the initial peak wavelength.

Table 5.1 List of refractive index of the binary mixture of BMIM-PF_6 and ethanol.

Molar fraction x	Molar concentration c (mol/L)	Refractive index *n*
0.4960	4.17	1.40171
0.5032	4.19	1.40193
0.5981	4.38	1.40432
0.7045	4.55	1.40639
0.8003	4.67	1.40790
0.9002	4.77	1.40930
0.9834	4.84	1.41052
1.0000	4.86	1.41069

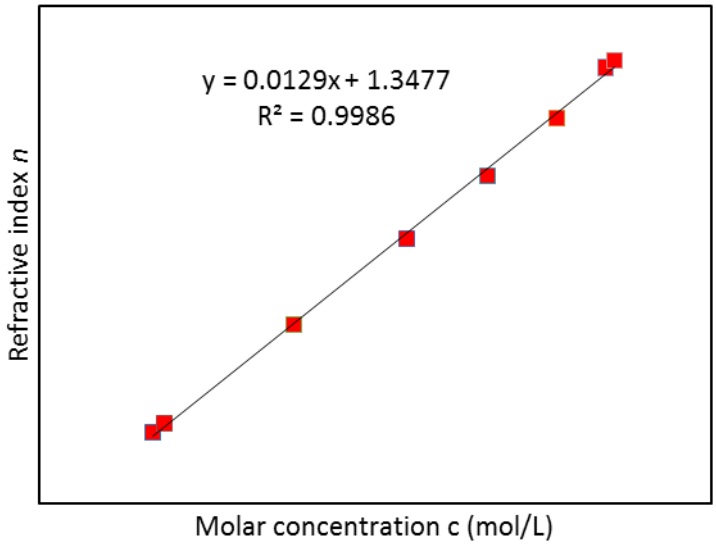

Fig. 5.5 Fitted linear relationship between the refractive index of mixture and the molar concentration of BMIM-PF_6.

5.2.2 Field model of ECTF using Nernst-Planck equation

The steady-state ion concentration in the FP cavity of optical tunable filters under a bias voltage can be calculated by simplifying the Nernst-Planck equation

$$\frac{\partial c}{\partial t} = \nabla \cdot \left[D\nabla c - \vec{\mathrm{u}}\, c + \frac{Dne}{k_B T} c \left(\nabla \phi + \frac{\partial \vec{\mathrm{A}}}{\partial t} \right) \right] \tag{5.14}$$

here t is time, D is the diffusion coefficient of the electrolyte ion, c is the concentration of the ion, and $\vec{\mathrm{u}}$ is the velocity of the fluid, n is the valence of ion, e is the elementary charge, k_B is the Boltzmann constant, T is the temperature, and $\vec{\mathrm{A}}$ is the external field. Eq. (5.14) is very complicated. Fortunately, in the steady state there are $\frac{\partial c}{\partial t} = 0$, $\vec{\mathrm{u}} = 0$ and $\frac{\partial \vec{\mathrm{A}}}{\partial t} = 0$. As a result, Eq. (5.14) can be simplified to be

$$\nabla \cdot \left[\nabla c + \frac{ne}{k_B T} c \nabla \phi \right] = \nabla^2 c + \frac{ne}{k_B T} c \nabla^2 \phi = 0 \tag{5.15}$$

$$\nabla^2 c - B_0 c \nabla^2 \phi = 0 \tag{5.16}$$

here B_0 is a constant given by $B_0 = \frac{ne}{k_B T}$. Now the expression is simple. To solve the concentration distribution c, it is necessary to find the electric potential ϕ.

5.2.2.1 Electric potential outside of an electric capacitor

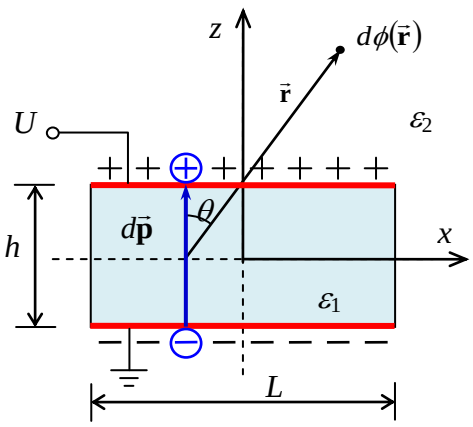

Fig. 5.6 Diagram for calculating the electric potential out of a capacitor.

Now we will try to find the electric potential outside of a rectangular capacitor, which has a length L (in the x direction), a width W (in the y direction) and a capacitor gap h (in the z direction). Fig. 5.6 shows one of its cross sections in the xz plane. The inner space of the capacitor has a permittivity ε_1 and the outer space has ε_2. The bias voltage U is applied across the capacitor, and positive charges accumulate on the top plate and negative ones on the bottom plate.

The capacitance C is

$$C = \frac{\varepsilon_1 LW}{h} \tag{5.17}$$

The charge density on the top and bottom is

$$\rho = \frac{CU}{LW} = \frac{\varepsilon_1}{h} U \tag{5.18}$$

Now consider the charges in an infinitesimal area $dudv$ of the capacitor generates. They generate a dipole

$$d\vec{\mathbf{p}} = (\rho dudv)(h\hat{\mathbf{z}}) = \rho h dudv\hat{\mathbf{z}} \tag{5.19}$$

here $\hat{\mathbf{z}}$ is the unit vector of z axis.

The contribution of this dipole to the electric potential at the position $\vec{\mathbf{r}}$ is given by

$$d\phi = k\frac{\vec{\mathbf{p}}\cdot\vec{\mathbf{r}}}{r^3} = k\rho h du dv \frac{\hat{\mathbf{z}}\cdot\vec{\mathbf{r}}}{r^3} = k\rho h \frac{z}{r^3} du dv \tag{5.20}$$

here $k = \dfrac{1}{4\pi\varepsilon_2}$.

The electric potential at $\vec{\mathbf{r}}$ can be expressed by

$$\phi = \int_{-W/2}^{W/2} dv \int_{-L/2}^{L/2} k\rho h \frac{z}{r^3} du k = k\rho h z \int_{-W/2}^{W/2} dv \int_{-L/2}^{L/2} \frac{1}{\left[(x-u)^2 + (y-v)^2 + z^2\right]^{\frac{3}{2}}} du \tag{5.21}$$

After a series of integration, the final result is

$$\begin{aligned}\phi = \frac{\varepsilon_1}{4\pi\varepsilon_2}\Bigg\{ &\arctan\left[\frac{(2x-L)(2y-W)}{2z\sqrt{(2x-L)^2+(2y-W)^2+z^2}}\right] \\ &-\arctan\left[\frac{(2x+L)(2y-W)}{2z\sqrt{(2x+L)^2+(2y-W)^2+z^2}}\right] \\ &+\arctan\left[\frac{(2x+L)(2y+W)}{2z\sqrt{(2x+L)^2+(2y+W)^2+z^2}}\right] \\ &-\arctan\left[\frac{(2x-L)(2y+W)}{2z\sqrt{(2x-L)^2+(2y+W)^2+z^2}}\right]\Bigg\}\end{aligned} \tag{5.22}$$

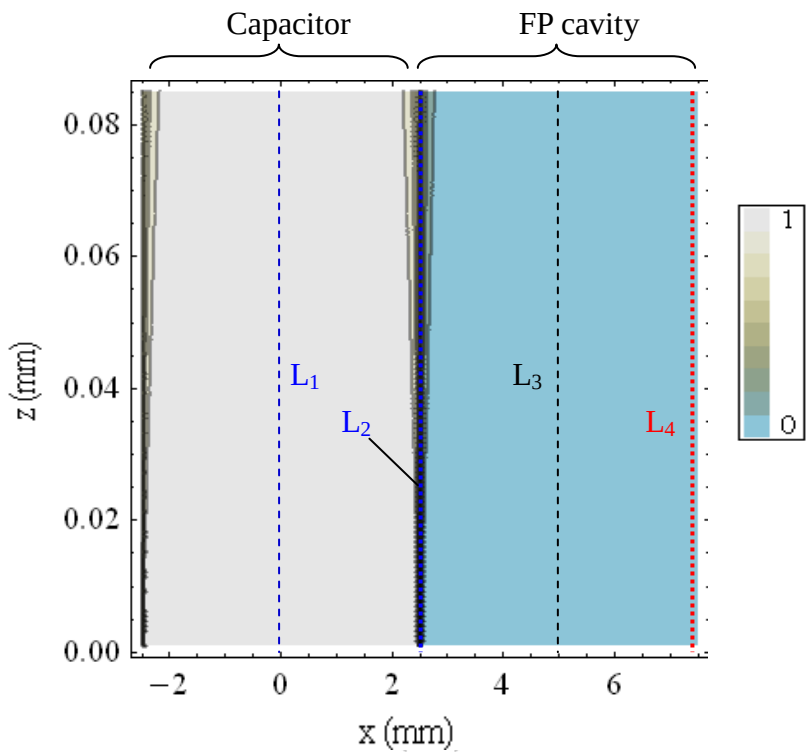

Fig. 5.7 Contour plot of the normalized electric potential outside of the parallel-plate capacitor (assuming y = 0). Here -2.5 mm ≤ x ≤ 2.5 mm corresponds to the region above the top plate of the capacitor, and 2.5 mm ≤ x ≤ 7.5 mm corresponds to the region of FP cavity. L_1, L_2, L_3 and L_4 represents four observation lines, L_1 is the central line of the capacitor, L_2 is the edge between the capacitor and the FP cavity, L_3 is the central line of the FP cavity, and L_4 is the outer edge of the FP cavity.

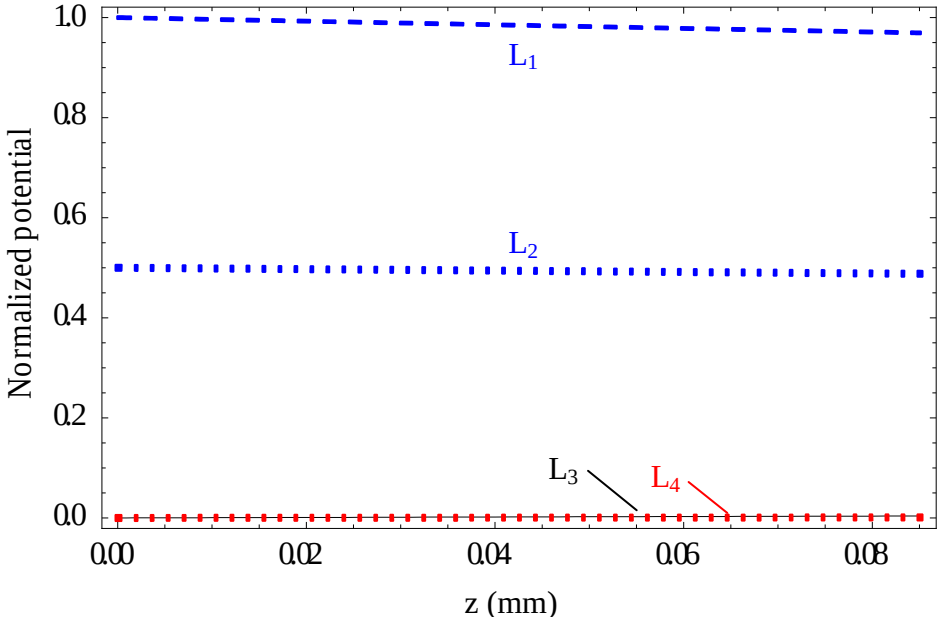

Fig. 5.8 Variations of the normalized electric potential along the observation lines.

5.2.2.2 Calculated results

Assume L = 5 mm, W = 5 mm, and the FP cavity is in the range of z = 0 to 0.085 mm. These are the parameters of real devices used for experimental studies. The normalized electric potential at the plane y = 0 is contoured in Fig. 5.7. In the actual device design, the region in between -2.5 and 2.5 mm corresponds to the space above the top plate of the capacitor, and that in between 2.5 and 7.5 mm is for the FP cavity. It is seen that the potential is strong over the capacitor, and the strong region bends in with the increase of the distance from the capacitor top plate. In contrast, the potential is small and almost uniform over most of the FP cavity.

Fig. 5.8 plots the variations of the normalized electric potential along different observation lines. It is seen that the curve for L_1 is close to 1 but decreases slightly with larger z; the curve for L_2 is close to 0.5 and decreases too. In contrast, the curves for

both L_3 and L_4 are very small (close to 0) but increases slightly with larger *z*. These trends are reasonable if we consider the capacitor as a collection of small electrical dipoles.

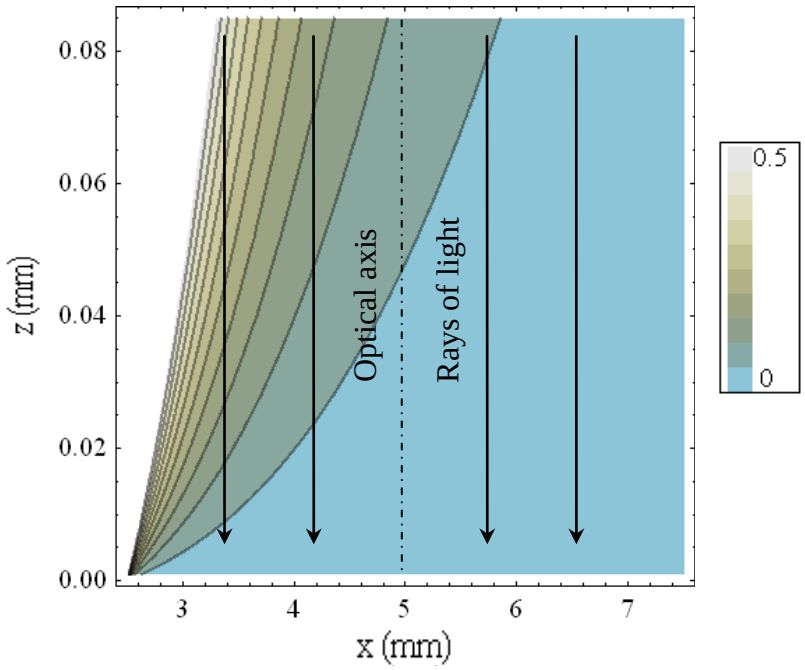

Fig. 5.9 Close-up of the electric potential distribution in the FP cavity region.

To see more details, a close-up of the potential distribution in the FP cavity region is contoured in Fig. 5.9. It is seen that there is still certain variation over the whole region. In the operation of the optical tunable filter, the rays of light go through the FP cavity along the *z* axis, it is thus more meaningful to examine the integrated potential along vertical lines, i.e.,

$$\Phi = \int_0^h \phi dz \tag{5.23}$$

here *h* is the cavity length of the FP cavity.

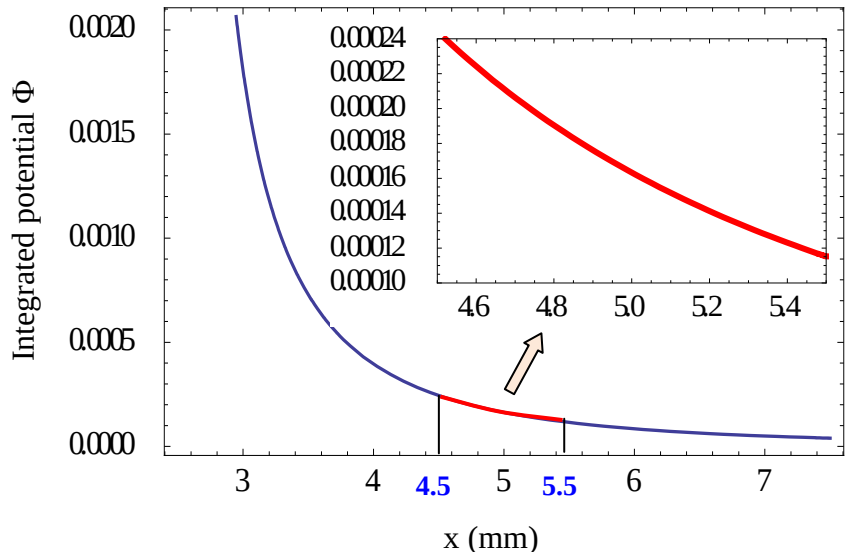

Fig. 5.10 Integrated potential along the z direction, which represents the total potential experienced by the rays of light that go through the FP cavity. The inset shows the close-up of the region 4.5 mm ≤ x ≤ 5.5 mm, which represents the region that is used for the collimated beam in the operation of tunable filters.

The integrated potential as a function of x is plotted in Fig. 5.10, which represents the total potential experienced by the rays transmitted at different locations. It can be seen that the integrated potential drops rapidly when it moves away from x = 2.5 mm (i.e., the edge between the capacitor and the FP cavity). After x = 4 mm, it becomes quite flat. In the operation of the tunable filters, the collimated beam has usually a beam diameter of about 1 mm, and thus the working region of the FP cavity is between 4.5 mm and 5.5 mm. The inset of Fig. 5.10 shows an enlarged view of this region. The integrated potential is changed from Φ = 0.00024 to 0.00010 when x goes from 4.5 mm to 5.5 mm. In comparison, the integrated potential is Φ = 1.15 at x = 0 mm (i.e., the central line of capacitor) and Φ = 0.58 at x = 2.5 mm (the edge between the capacitor

and the FP cavity). Therefore, the drop Φ = 0.00024 to 0.00010 is very small and thus the variation is of little significance.

Based on this, we can conclude that the electric potential in the working region (4.5 mm $\leq x \leq$ 5.5 mm) of the FP cavity is negligibly small and can be simply treated as $\phi \approx$ 0. Substituting Φ = 0 into Eq. (5.16), one of the solutions is that

$$c = \text{constant} \tag{5.24}$$

This shows the simple model is a good estimation in the region of interest (i.e., 4.5 mm $\leq x \leq$ 5.5 mm).

In fact, the combined use of Eq. (5.16) and (5.22) with proper boundary condition could give more precise results. However, the boundary conditions are complicated to define. Therefore, we will use the simple model for analysis and for comparison with experimental results.

5.3 Design and Fabrication

5.3.1 Sputtering deposition

Magnetron sputtering is a physical vapor deposition (PVD) for coating (see Fig. 5.11). Generally, it works under a relatively stable vacuum state; when the glow discharge plasma is generated between the anode and the cathode, the energetic ions from the plasma bombard the target plate at the cathode to eject atoms from the target. Then, the atoms are condensed onto the substrate as a thin film. Apart from the atoms, secondary electrons also come out of the target surface to act as the ion bombardment for maintaining the plasma [38].

To control the properties of thin film, some parameters should be controlled,

including the sputtering current, the chamber pressure, the target to substrate distance, the substrate temperature, the gas mixture and the applied voltage. The sputtering current determines the deposition rate of the thin film on the substrate. The substrate temperature affects the crystallinity and the density of thin film. For instance, it is necessary to increase the temperature above 300 ℃ to grow an ITO thin film on a glass substrate [39]. For the chamber pressure, it determines the mean free path for the sputtered materials. The target to substance distance, together with the chamber pressure, would affect the porosity, the crystallinity and the texture of the thin film.

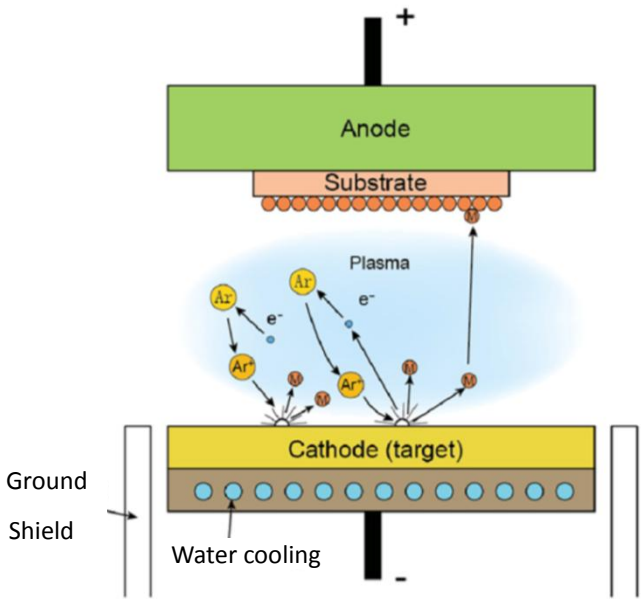

Fig. 5.11 Working principle of magnetron sputtering [40].

5.3.2 Thin film deposition

There are many processes for thin film deposition methods, for instance, chemical vapor deposition (CVD), plasma laser deposition (PLD), DC/RF magnetron sputtering, etc.

The layer structure of ECTF is shown in Fig. 5.12. In this experiment, the DC

magnetron sputtering is used for depositing ~20 nm thick gold (Au) thin film on the mirror and RF magnetron sputtering is used for depositing ~50 nm thick silver (Ag) thin film, which is then covered by a ~150 nm thick SiO_2. And the thickness of the thin films is verified by surface profiler. As the adhesion between mirror and Au or Ag to SiO_2 is not good enough, an adhesion layer of Cr is deposited on the mirror before coating the Au thin film [41,42].

The adhesion of thin films on mirrors are very importance since thin films need to be soaked into electrolyte solution, poor adhesion of thin films would cause the thin films to fall off during experiment. Hence, before DC / RF sputtering, some physical work should be done; for example, the mirrors can be washed thoroughly by ultrasound cleaning to remove any dust or grease.

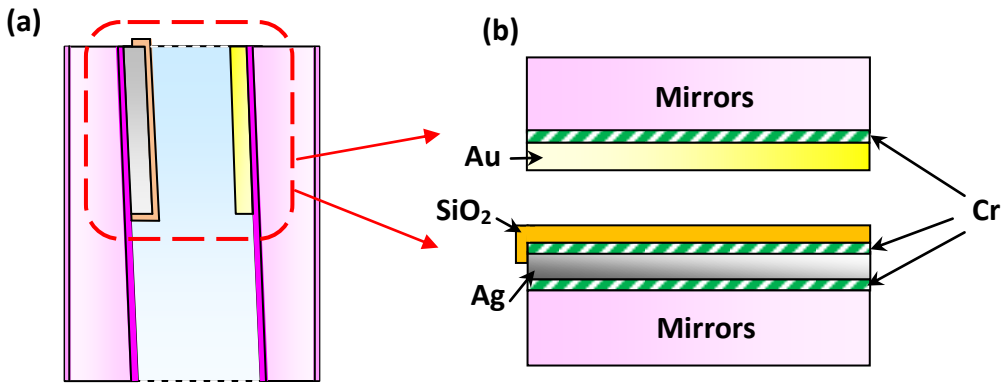

Fig. 5.12 Cross-section of the structure of ECTF. (a) The overall structure of ECTF, (b) layers in the capacitor region.

5.3.3 Fabrication of electrolyte-capacitor tunable filters

After the two mirrors were aligned to be parallel, the FP resonant cavity was filled with BMIM-PF_6 ionic liquid. BMIM-PF_6 is a room temperature ionic liquid (RTILs), which offers good electrical conductivity, high ionic mobility and thermal stability property [43]. Moreover, it has high transmission at 1550 nm. Therefore, it was used in this experiment. At the beginning, it allowed a comb of wavelength to pass through the TF. When a bias voltage was applied to the electrodes, an electric field was built up across the SiO_2 dielectric layer and the gold (Ag) electrode, the $[PF_6]^-$ ions were attached to the positive electrode (capacitor part). As a result, the ion concentration on the uncoated transparent parts reduced accordingly, leading to a variation of refractive index and hence the OPL of tunable filters.

5.4 Brief introduction of physical and chemical properties of electrolyte solutions

In this experiment, four different types of electrolyte solutions were tried, including simple electrolyte solution (NaCl), conductive polymer solution (PEDOT), ionic solution (BMIM-PF_6) and Nafion [44,45]. In the next chapter, the performance of each type of electrolyte solution will be tested and compared.

5.4.1 Sodium Chloride (NaCl) solution

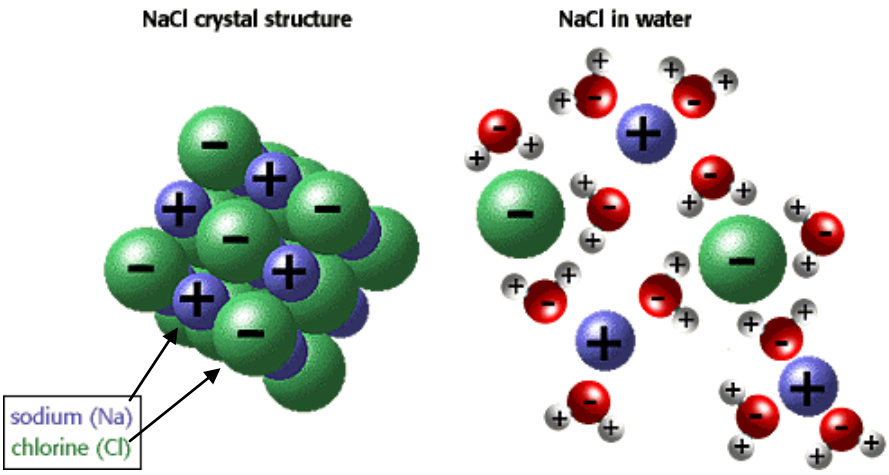

Fig. 5.13 The solid state and aqueous state of sodium chloride [46].

Sodium chloride (NaCl) crystal structure is well packaged with sodium (Na^+) and chloride (Cl^-) ions together. Because of the ions are regularly packed and held with ionic bonding, there are no free mobile ions. Thus solid NaCl is a non-conductive material. However, it is soluble in water but insoluble or slight soluble in most liquids. When they are dissolved into water, the ions can move freely. Therefore, NaCl solution can conduct electricity.

5.4.2 Poly (3, 4-ethylenedioxythiophene) (PEDOT)

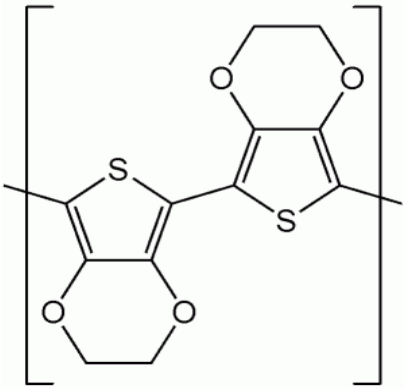

Fig. 5.14 The molecular structure of the PEDOT polymer.

Poly(3,4-ethylenedioxythiophene) (PEDOT) is one of the intrinsically conductive polymers. It is dark black in room temperature, with high viscosity and thermal stability. The thickness of PEDOT would affect the optical transmittance. It is suggested that when the thickness of PEDOT is below 400 nm, the optical loss would be less than 0.5 dB at λ = 1550 nm. However, when it is thicker than 400 nm, the insertion loss would be increased significantly [47].

5.4.3 1-Butyl-3-methylimidazolium hexafluorophosphate (BMIM-PF_6)

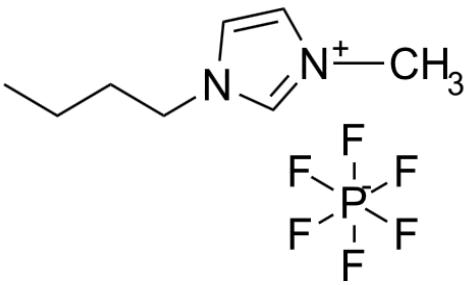

Fig. 5.15 The molecular structure of BMIM-PF_6.

1-Butyl-3-methylimidazolium hexafluorophosphate (BMIM-PF_6) is composed of $[BMIM]^+$ and $[PF_6]^-$ and is one of the common room temperature ionic liquid (RTIL) with its melting point close to the room temperature. As they are usually high in thermal conductivity, high viscosity and the range of temperature is wide, RTILs have lots of beneficial properties for industrial applications, including heat transfer fluids, electrolytic media for dye-sensitized solar cell [48,49]. Since the RTILs are entirely consists of anions and cations, which is suitable for using it in the FP cavity.

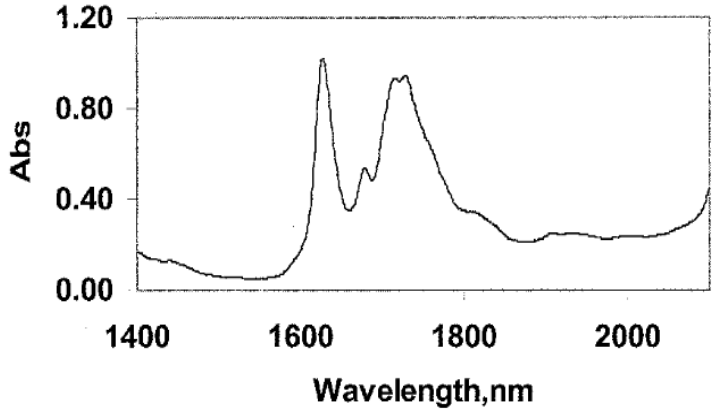

Fig. 5.16 The absorption spectrum of BMIM-PF6 electrolyte solution [50].

In optical area, BMIM-PF6 offers a low absorption at λ=1550nm which would give out a high transmission and low insertion loss to the performance of ECTF (see Fig. 5.15).

5.4.4 Sulfonated tetrafluoroethylene based fluoropolymer-copolymer (Nafion)

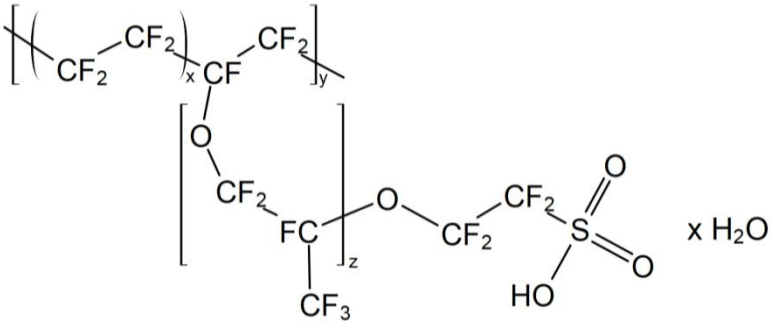

Fig. 5.17 The molecular structure of Nafion.

Sulfonated tetrafluoroethylene based fluoropolymer-copolymer (Nafion) is commonly found in fabrication of fuel cell by making it as an electrolyte membrane. It functions as a Photon Exchange Membrane (PEM) by allowing the photons or cations pass through PEM only.

5.5 Similarities and differences of ECTF with electrochromic window

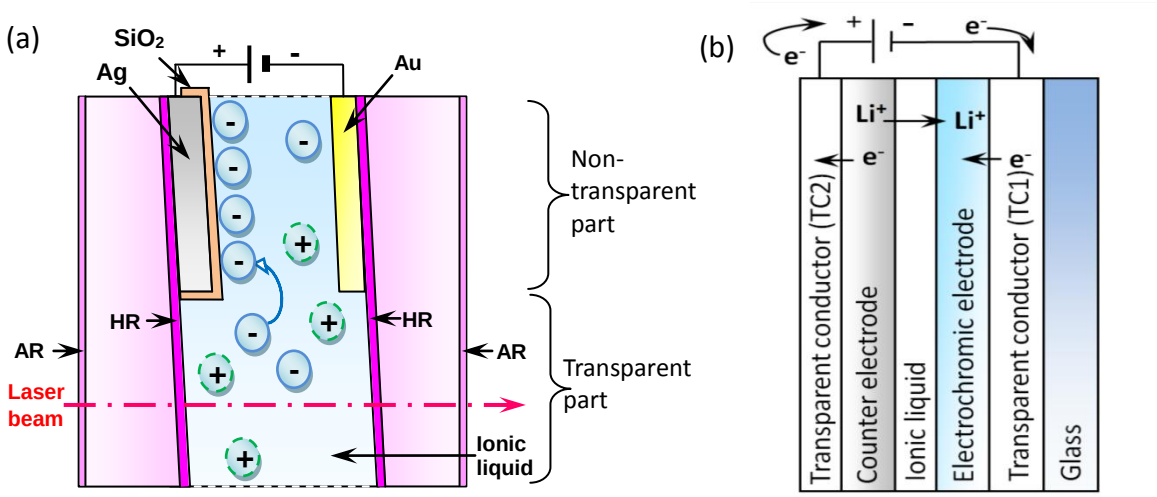

Fig. 5.18 Working principle of two devices. (a) Electrolyte-capacitor tunable filter (ECTF); (b) Electrochromic window.

There are some similarities and differences between these two devices which are based on their structures, working principles, physical appearances and applications. Mainly, they have similar structures since both of them consist of ionic liquid, a couple of conductive layers and a layer for storage of charges.

However, their working principles, physical appearance and application are totally different. For the ECTF, when a bias voltage is applied to the ECTF, an E-field is built up across the electrode parts, negative ions are then attracted to the dielectric layer, and hence the concentration of ionic liquid is varied so as to tune the central wavelength and it does not involved any chemical reaction within the whole process (Fig. 5.18(a)). On the other hand, when a bias is applied to the electrochromic window, a voltage drives to the counter electrode (storage of charge) and the lithium ions move to the

electrochromic electrode. The ionic liquid only works as a medium for the migration of lithium ions (see Fig. 5.18(b)). It then undergoes an oxidation which changes the electrochromic layer from a clear state into tinted state.

For the physical appearance, half of the ECTF are opaque which is used for the wavelength tuning while another half of the ECTF are transparent for the propagation of light. However, for the electrochromic window, the whole window is transparent in normal situation. Once a bias is applied, the entire window is tinted but when the applied voltage is removed, the window becomes transparent again.

For the application, ECTFs are supposed to be used as a wavelength tunable filter by transmitting a necessary wavelength from a comb of wavelengths and which can also be used in the microfluidics system. However, the electrochromic window is used to absorb sunlight when it is tinted and provide privacy to the indoor.

Chapter 6

Experimental Results and Characterization of Electrolyte-Capacitor Tunable Filters

In this chapter, the experimental results, including the tuning property and the dynamic response of the electrolyte-capacitor tunable filters, will be presented. Moreover, four types of electrolyte solutions will be filled into the FP cavity to test their tuning capabilities.

6.1 Experimental results

6.1.1 Tuning range of tunable filters

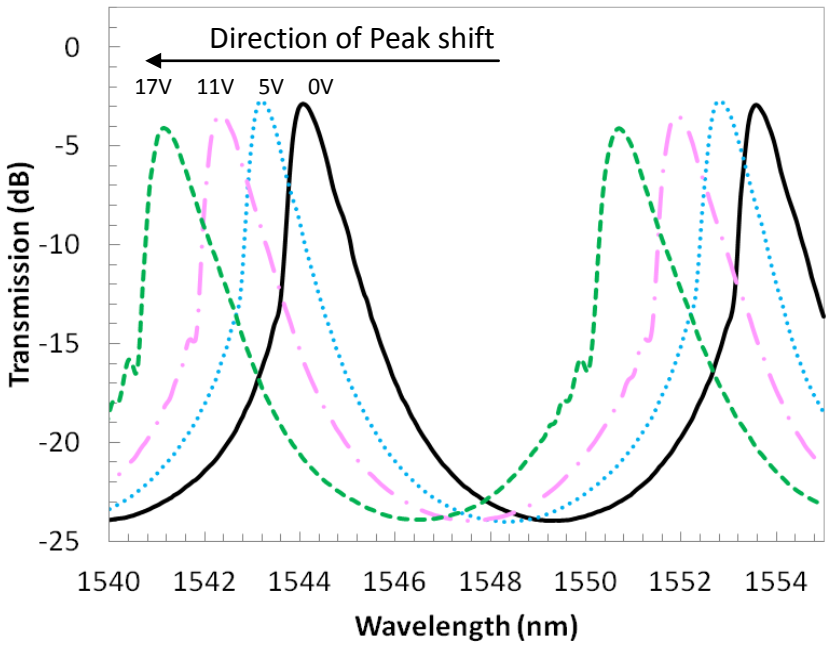

Fig. 6.1 Shift of transmission spectra of the tunable filters filled with BMIM-PF_6 solution under different bias voltage.

The measured peak shift of the transmission spectra of tunable filter under different bias voltage was measured as shown in Fig. 6.1. The full spectral range, the insertion loss and the contrast of the tunable filters are about 10 nm, 2.4 dB and 23 dB, respectively. The 0.5 and 3 dB bandwidths are 0.35 nm and 0.6 nm, respectively. Moreover, the transmission peak of the filters can be tuned from 1541.2 nm to 1544.2 nm when the bias voltage was tuned from 0 to 17 V.

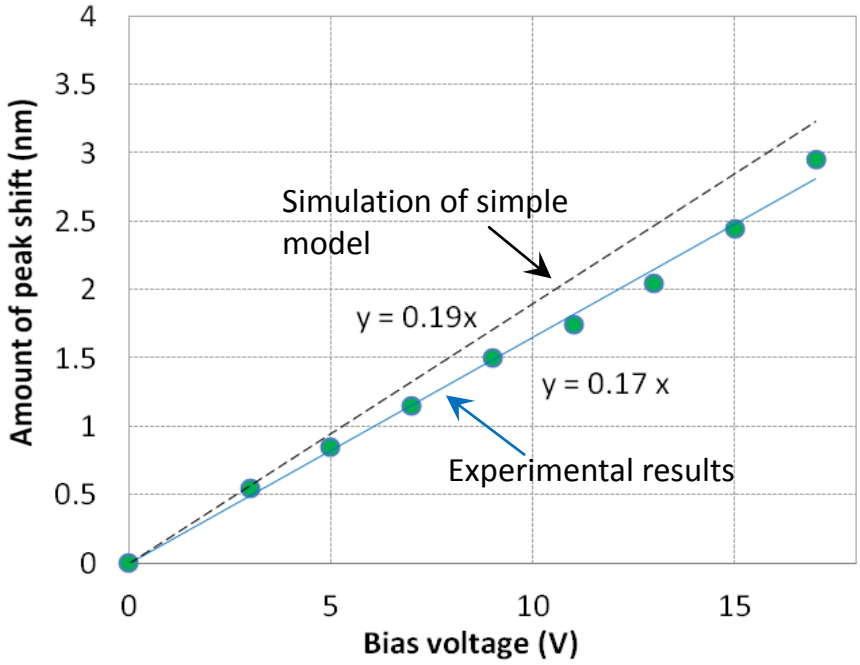

Fig. 6.2 Peak shift of the ECTF as a function of bias voltage.

Fig. 6.2 plots the peak shift as a function of the bias voltage. The blue curve shows the experimental result while the black dashed line shows the simulated result using Eq. (5.13) (i.e., the simple model). In the experimental curve, the slope is about 0.17 nm/V within a bias of 0—17 V. According to Fig. 5.13, the simulated curve has a slope of 0.19 nm/V. It is close to the experimental slope of 0.17 nm/V. This shows that the simple model is valid and easier to be used than the field model.

6.1.2 Dynamic response of tunable filters

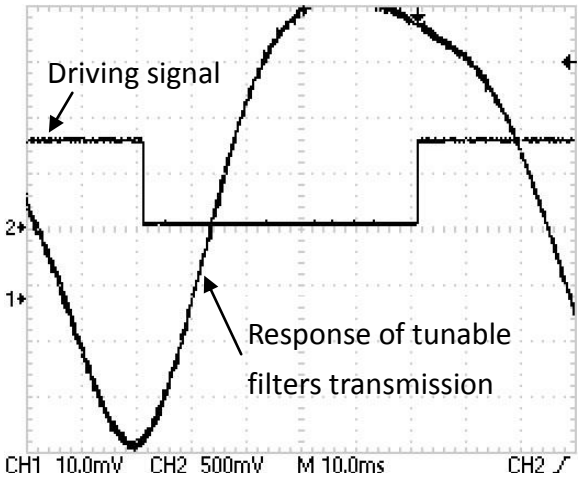

Fig. 6.3 Dynamic response of the electrolyte-capacitor tunable filters.

The setup for measuring the dynamic response of the ECTF is similar to that of the PZT-TF in Fig. 4.4. The dynamic response of ECTF is shown on Fig 6.3. A square wave of 0－1.5 V with a period of 100 ms was applied to the electrodes. The rise time is about 30 ms and the fall time is about 40 ms.

6.2 Other characteristics

6.2.1 Analysis of interference pattern on mirrors

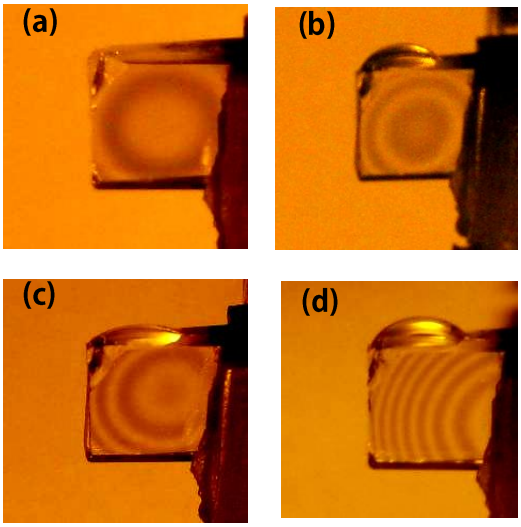

Fig. 6.4 Interference patterns of tunable filters under the bias voltage of (a) 0 V ,(b) 5 V , (c) 11 V , (d) 17 V.

Fig. 6.4 shows the observed interference fringes formed by the two mirrors under different bias voltages. Before applying any bias voltage to the TF, the circular Newton rings appears in the middle of the mirrors which indicates a good parallelism of two mirrors (Fig. 6.4(a)). Under the bias voltage, more fringes appeared, the ions started to migrate to the electrode parts. It induced an increased gradient of refractive index, but the parallelism of mirrors remained unchanged (Fig. 6.4(b)). When the bias voltage went higher, the center of the Newton rings was shifted slightly to the electrode sides, the gradient of refractive index became larger as shown in Fig. 6.4(c). Further increasing the bias voltage would cause a large amount of ions move suddenly to the electrode sides. The density of interference fringes was increased quickly and

the parallelism of the mirrors was also affected. This caused not only a fluctuation of transmission spectrum, but also an increase of insertion loss (Fig. 6.4(d)).

6.2.2 Effects of different electrolyte solutions used in the FP cavity

Table 6.1 summarizes the effect on different electrolyte solutions used in the FP cavity. There were four types of electrolyte solutions: 1-Butyl-3-methylimidazolium hexafluorophosphate (BMIM-PF_6) ionic liquid solution [50], 0.1-M sodium chloride (NaCl) electrolyte, Poly (3,4-ethylenedioxythiophene) (PEDOT) conductive polymer [52] and sulfonated tetrafluoroethylene based fluoropolymer-copolymer (Nafion) solution [53]. To fabricate an effective OTF, many specifications such as the sensitivity, the insertion loss, the contrast and the drifting of transmission spectrum should be considered. Among these four electrolytes, the sensitivity and the drift of PEDOT was the best and smallest (Table 6.1), however, as the physical appearance of PEDOT is dark black, it would absorb the laser beam (1550 nm). Although a few nanometers thick of PEDOT are transparent to near infrared source [46], the limitation of a FP cavity should be larger than micrometers. Therefore, using PEDOT as an electrolyte solution in a micrometer thick FP cavity, it would exhibit a large insertion loss (~ 25 dB), and a small contrast (~ 5 dB) and is not a suitable electrolyte for the FP tunable filters. Despite the PEDOT had a large tuning sensitivity (10 nm/V), BMIM-PF_6 is more suitable than PEDOT, though its sensitivity (0.17 nm/V) is smaller than PEDOT.

Apart from the PEDOT solution, 0.1-M NaCl electrolyte and Nafion solution were tried as well. Compared with those of the BMIM-PF_6 solution, their performances were similar, having low sensitivity, moderate insertion loss but large drift (~10 nm). For BMIM-PF_6 and water, the viscosity of BMIM-PF_6 is higher than that of water by about

1000 times [50,54]. Therefore, it reduces the possibility of BMIM-PF_6 flowing way from the FP cavity. Furthermore, due to the unique chemical and physical properties of ionic liquid electrolyte, BMIM-PF_6 is stable in air and moisture environment. According to [50], BMIM-PF_6 can only absorb 8.3×10^{-2} M of water in 24 hours. As a result, BMIM-PF_6 yields a low drift (~0.2 nm)

From the above analysis, NaCl and Nafion solution were not suitable for the FP cavity. BMIM-PF_6 ionic liquid achieved the best performance for the tunable filters. More specifically, it had the lowest insertion loss (2.4 dB), a relatively large SMSR (23 dB) and a good stability (drift < 0.2 nm), which are essential for a good optical tunable filter.

Table 6.1 Characteristics of different electrolyte solutions filled in the FP cavity.

Material in FP cavity	**Sensitivity (nm/V)**	**Insertion loss (dB)**	**SMSR (dB)**	**Drift (nm)**
BMIM-PF_6 ionic liquid	0.17	2.4	23	< 0.2
0.1 M NaCl electrolyte	0.1	10	25	10
PEDOT conductive polymer	10	25	6	< 0.1
Nafion solution	0.2	8	20	10

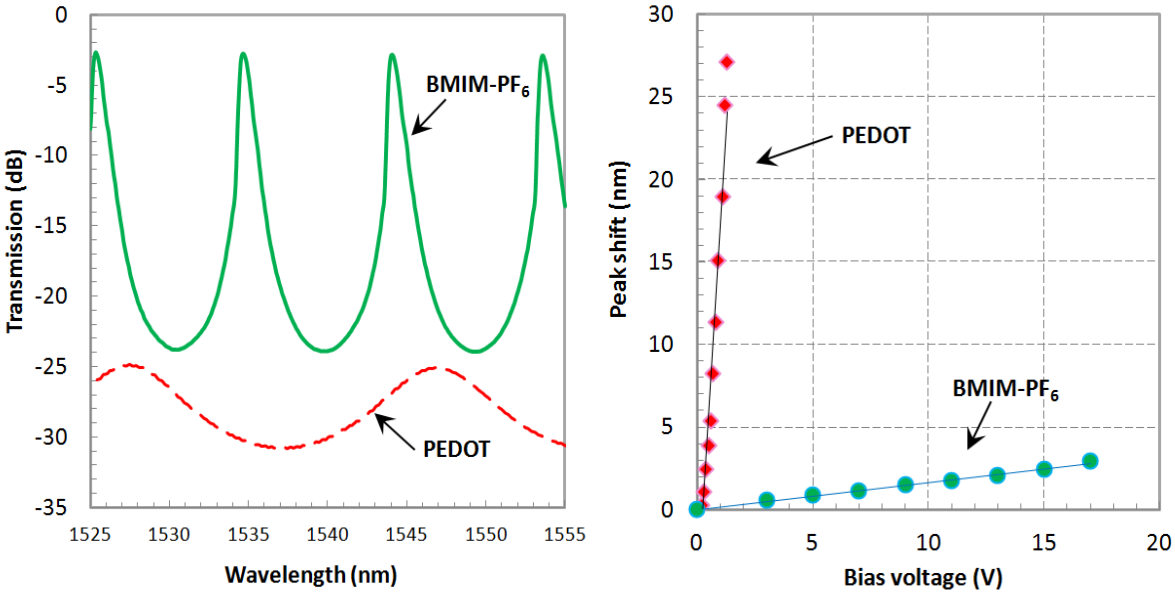

Fig. 6.5 Graphs of ECTF filled with BMIM-PF6 electrolyte solution and PEDOT in the FP cavity respectively. (a) Transmission spectra of ECTF at 0 V; (b) peak shift of ECTF as a function of bias voltage.

6.3 Problems

As the ECTFs are filled with liquid inside the cavity, it is difficult for packaging and it is dynamically unstable. Besides these technological challenges, the main problems found with ECTFs are drainage of solution, poor adhesion of thin film deposition and the instability of dynamic response. These problems will be discussed in detail.

6.3.1 Drainage of solution

During the experiment, it is observed that the solutions gradually dry up in the FP cavity, especially for the NaCl and Nafion solutions. The wording “drainage” in this chapter defines as leakage and drying up. After a few hours, the amounts of NaCl solution and Nafion solution decrease sharply. This may be due to the low adsorption ability between the mirror glasses and the solutions, and may also result from the evaporation of solution. The viscosities of NaCl and Nafion are low among four electrolyte solutions, the drifting problem is serious. These two electrolyte solutions are not suitable for the FP cavity.

6.3.2 Poor adhesion of thin films on mirrors

In addition to the drainage problem, the adhesion of thin film is not strong enough. When it is soaked into the solution and the bias is applied to the electrode, the Ag and SiO_2 thin films are often peeled off after several experiments. Poor adhesion occurs between the Ag film and the mirror glass, though a Cr adhesion layer is deposited.

6.3.3 Instability of dynamic response

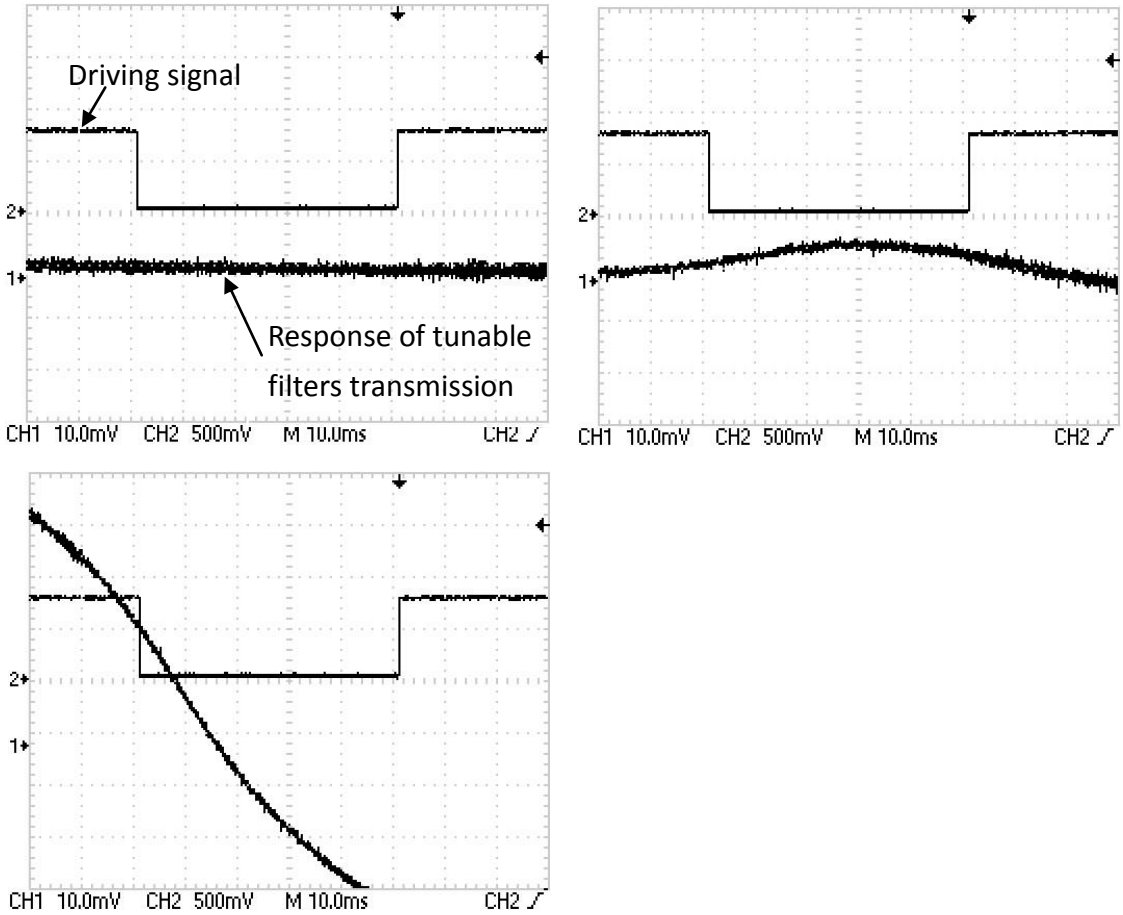

Fig. 6.6 Dynamic responses of the electrolyte-capacitor tunable filter.

Fig. 6.6 shows the dynamic responses under almost the same square-wave bias. It is seen that the dynamic response varies significantly such instability might be due to the drainage and evaporation. Further investigation is needed to study the actual reasons.

Chapter 7

Conclusions and Recommendations

7.1 Conclusions

In this project, two types of Fabry-Pérot tunable filters have been designed, fabricated and characterized. The achieved performances are summarized in Table 7.1. In the first part of my research study, the PZT-actuated tunable filter has been developed, which achieves a tuning sensitivity of ±1 nm/V, a tuning range of 80 nm, a tuning speed of 1 ms and an insertion loss of 1.0 dB. By redesigning the structure, the latest PZT tunable filters have improved performance in the aspects of insertion loss, strength and stability.

In the second part of the study, an electrolyte-capacitor tunable filter is developed using a new method for wavelength tuning. Among these four electrolyte solutions that have been tried, BMIM-PF_6 achieves the best performance; the insertion loss and the contrast ratio are 2.4 dB and 23 dB, respectively. Although the performance has a lot to improve, this tunable filter demonstrates a new working principle and may be applicable to the microfluidic systems that require on-chip optical filters in fluidic environment, such as a bio-sensing device. Particularly, this electrolyte-capacitor tuning method features no mechanical movement and it can be integrated with microfluidics.

Table 7.1 Main specifications of PZT and electrolyte-capacitor tunable filters.

	PZT tunable filter	Electrolyte-capacitor tunable filter
Tuning Sensitivity (nm/V)	1	0.17
Tuning Range (nm)	80	3
Tuning Speed (ms)	1	30
Insertion loss (dB)	1.0	2.4

7.2 Recommendations for future work

In the electrolyte-capacitor tunable filters that use BMIM-PF_6 solution, the transmission spectrum is not stable. Hence, it is suggested that the FP cavity should be sealed with UV adhesive, which provides low strength to the mirror and helps to maintain a good parallelism of two mirrors, after it is filled with the electrolyte solution. In this way, the drainage problem would be reduced and the spectral drift problem could be alleviated.

Besides of the drainage problem, the poor adhesion of thin film affects the experiment seriously. When it is soaked into the solution, the Ag and SiO_2 thin films are often peeled off after several experiments. Although an adhesion Cr layer is deposited between the Ag and SiO_2 layers, the SiO_2 thin film often detaches from the Cr thin film. Therefore, the structure of electrolyte capacitor is spoiled. To tackle this problem, it is suggested that the substrate (i.e., the mirror glass) should be cleaned thoroughly to remove any contamination before depositing the thin films [55]. And new materials for adhesion layers, the transparent conductive Indium Tin Oxide (ITO), could be tried.

Moreover, the dynamic response of ECTF is not stable and it might be solved by sealing the ECTF. The detailed reasons are worth further study.

Although the PZT actuated tunable filter performs a large tuning ability, when it is combined with the ECTF to become a hybrid (PZT/EC) OTF device, it might produce some unexpected outcome. For instance, it might overcome the peak shifting ability when a positive bias is applied to the hybrid OTF, the PZT and the EC might perform oppositely and the peak shifting would be cancelled out or decreased in shifting ability. Therefore, only changing one parameter (either the cavity length or the refractive index of material used in FP cavity) is enough to attain the wavelength tuning.

Bibliography

[1] H. Ishii, K. Kasaya and H. Oohashi, "Wavelength-tunable lasers for next-generation optical networks," *NTT technical Review*, vol. 9, no. 3, pp. 1-6, 2011.

[2] J. Elmirghani and H. T. Mouftah, "Technologies and architectures for scalable dynamic dense WDM networks," *Communications Magazine,* vol. 38, no. 2, pp. 58-66, 2000.

[3] G. E. Keiser, "A review of WDM technology and applications," *Optical Fiber Technology,* vol. 5, no. 1, pp. 3-39, 1999.

[4] J. Missinne and B. V. Hoe, "Artificial shin based on flexible optical tactile sensors," *SPIE Newsroom,* pp. 1-3, 2010.

[5] Questex Media Group, Inc., "Tunable lasers for multichannel fiber-optics sensors," http://archives.sensorsmag.com/articles/0803/28/main.shtml.

[6] G. Ducournau, O. Latry and M. Ketata, "Fiber based Mach-Zehnder interferometric structures: principles and required characteristics for efficient modulation format conversion," in *Passive Components and Fiber-based Devices II*, Shanghai, China, 2005.

[7] E. L. Wooten, R. L. Stone, E. W. Miles and E. M. Bradley, "Rapidly tunable narrowband wavelength filters using LiNbO3 unbalanced Mach-Zehnder interferometers," *Journal of Lightwave Technology,* vol. 14, no. 11, pp. 2530-2536, 1996.

[8] J. L. Jackel, P. Perlmutter and J. Johnson, "High-speed low-voltage modulation with a nonsymmetric Mach-Zehnder interferometer," *Jorunal of Lightwave Technology,* vol. 7, no. 6, pp. 937-940, 1989.

[9] A. L. Washburn and R. C. Bailey, "Photonics-on-a-chip: recent advances in integrated waveguides as enabling detection elements for real-world, lab-on-a-chip biosensing applications," *Analyst,* vol. 136, no. 2, pp. 227-236, 2011.

[10] J. C. Wyant, "Multiple Beam Interference," http://wyant.optics.arizona.edu.

[11] J. M. Vaughan, The Fabry-Pérot interferometer history, theory, practice and applications, United Kingdom: Adam Hilger,Bristol and Philadelphia, 1989.

[12] J. F. James and R. S. Sternberg, The design of optical spectrometers, Britain: Chapman and Hall, 1969.

[13] G. Schulz and J. Schwider, "Precise measurement of planeness," *Applied Optics,* vol. 6, no. 6, pp. 1077-1087, 1967.

[14] A. J. Francis and E. W. Harvey, Fundamentals of optics, New York: McGraw-Hill, 1976.

[15] M. Born and E. Wolf, Principles of optics (4th edition), Pergamon Press, 1970.

[16] Nikon, "Principles and applications of multiple-beam interferometer," http://www.microscopyu.com/articles/interferometry/multibeam.html.

[17] S. H. Song, "Interference of light," http://optics.hanyang.ac.kr.

[18] H. Ishio, J. Minowa and K. Nosu, "Review and status of

wavelength-division-multiplexing technology and its application," *Journal of Lightwave Technology,* vol. 2, no. 4, pp. 448-463, 1984.

[19] M. Iodice, G. Cocorullo, F. D. Corte and I. Rendina, "Silicon Fabry-Pérot filters for WDM systems channels monitoring," *Optics communications,* vol. 183, no. 5, pp. 415-418, 2000.

[20] G. Cocorullo et al., "Simple and low-cost silicon Fabry-Pérot filters for WDM channel monitoring." Electronic-Enhanced Optics, Optical Sensing in Semiconductor Manufacturing, Electro-Optics in Space, Broadband Optical Networks," in *Digest of the LEOS Summer Topical Meetings*, IEEE, 2000.

[21] S. S. Yun and J. H. Lee, "A micromachined in-plane tunable optical filters using the thermo-optic effect of crystalline silicon," *Journal of Micromech and Microeng.*, vol. 13, pp. 721-725, 2003.

[22] A. T. Schremer and C. L. Tang, "External-cavity semiconductor laser with 1000 GHz continuous piezoelectric tuning range," *Photonics Technology Letter, IEEE,* vol. 2, no. 1, pp. 3-5, 1990.

[23] N. Wang, M. Feng, Z. Q. Feng, M. Y. Lam, L. Gao, B. Chen, A. Q. Liu and X. M. Zhang, "Narrow-linewidth tunable lasers with retro-reflective external cavity," *IEEE Photonic Technology Letters,* vol. 24, no. 18, pp. 1591-1593, 2012.

[24] A. Sneh and K. M. Johnson, "High-speed continuously tunable liquid crystal filters for WDM networks," *Journal of Light Technology,* vol. 14, no. 6, pp. 1067-1080, 1996.

[25] D. Taber, J. A. Davis, L. A. H. Jr and O. Almagor, "Optically controlled

Fabry-Pérot interferometer using a liquid crystal light valve," *Applied optics,* vol. 29, no. 17, pp. 2623-2631, 1990.

[26] P. L. Chen et al., "Analysis of a liquid crystal Fabry-Pérot etalon filters: A novel model.," *IEEE Photonics Technology Letters,* vol. 9, no. 4, pp. 467-469, 1997.

[27] K. Hirabayashi, H. Tsuda and T. Kurokawa, "Narrow-band tunable wavelength-selective filters of Fabry-Pérot interferometers with a liquid crystal intracavity," *IEEE Photonics Technology Letters,* vol. 3, no. 3, pp. 213-215, 1991.

[28] D. Hohlfeld, M. Epmeier and H. Zappe., "Tunable thermo-optic filters for WDM applications.," in *The Fifteenth IEEE International Conference*, IEEE, 2002.

[29] D. Hohlfeld and H. Zappe, "An all-dielectric tunable optical filters based on the thermo-optic effect," *Journal of optics A: Pure and applied Optics,* vol. 6, no. 6, p. 504, 2004.

[30] PIEZO System, Inc., "Introduction to Piezo transducers," http://www.piezo.com/tech2intropiezotrans.html.

[31] C.-Y. Chen et al., "Liquid-crystal based terahertz tunable Lyot filters," *Applied physics letters,* vol. 88, no. 10, pp. 101-107, 2006.

[32] J. S. Patel and M. W. Maeda., "Tunable polarization diversity liquid-crystal wavelength filters," *IEEE Photonics Technology Letters,* vol. 3, no. 8, pp. 739-740, 1991.

[33] D. Sadot and E. Boimovich, "Tunable optical filters for dense WDM networks," *IEEE Communication Magazine,* vol. 36, no. 12, pp. 50-55, 1998.

[34] W. Storr, “Types of Capacitor,” Basic Electronics Tutorials, http://www.electronics-tutorials.ws/capacitor/cap_2.html.

[35] Ceramic Industry, “Special Report/Glass manufacturing: Dynamic Views” http://www.ceramicindustry.com/articles/special-report-glass-manufacturing-dynamic-views.

[36] A. K. Ghatak, Optics (4th edition), United States: McGra-Hill, 2009.

[37] A.B. Pereiro, A. Rodríguez , "Study on the phase behavior and thermodynamic properties of ionic liquids containing imidazolium cation with ethanol at several temperatures," J. Chem. Thermodynamics 39 (2007) 978–989.

[38] D. G. Constantin, “Magnetron Sputtering Technique used for coating deposition; Techologies and Applications,” in *The 7th International Conference on Materials Science and Engineering-BRAMAT 2011*, Brasov, 2011.

[39] J. H. Lee, “Effects of substrate temperature on electrical and optixal properties ITO films deposited by rf magnetron sputtering,” *Journal of electroceramics*, vol. 23, no. 2-4, pp. 554-558, 2009.

[40] Direct Vacuum, “Magnetron Sputtering Technology,” http://www.directvacuum.com/sputter.asp.

[41] B. Moazzez, S. M. O'Brien and E. F. Merchrod. S., “Improved Adhesion of Gold Thin Films Evaporated on Polymer Resin: Applications for Sensing Surfaces and MEMS,” *Sensors*, vol. 13, no. 6, pp. 7021-7032, 2013.

[42] M. A. George et al., “Electrical, spectroscopic, and morphological investigation of cheomium diffusion through gold films,” *Thin solid films*, vol. 189, no. 1, pp.

59-72, 1990.

[43] Y. Qiao et al, "Sensities and viscosities of [BMIM][PF6] and binary systems [BMIM][PF6]+ ethanol, [BMIM][PF6]+ benzene at several temperatures and pressures: determined by the falling-ball method.," *Journal of Chemical & Engineering Data,* vol. 56, no. 5, pp. 2379-2385, 2011.

[44] H. Tang et al., "A degradation study of Nafion proton exchange membrane of PEM fuel cells," *Journal of Power Sources,* vol. 170, no. 1, pp. 85-92, 2007.

[45] K. Broka and P. Ekdunge, "Oxygen and hydtogen permeation properties and water uptake of Nafion(R) 117 membrane and recast film for PEM fuel cell.," *Journal of Applied Electrochemistry,* vol. 27, no. 2, pp. 117-123, 1997.

[46] P. P. Shapley, "Concnetration," University of lllinois, 2011. http://butane.chem.uiuc.edu/pshapley/genchem1/l21/1.html.

[47] J. D. Zhang et al., "Towards the improvement of attenuation range and response time of electrochromic polymer-based variable optical attenuators," *Optical Materials,* vol. 27, no. 2, pp. 265-268, 2004.

[48] B. Li et al., "Review of recent progress in solid-state dye sensitized solar cells," *Solar Energy Materials and Solar Cells,* vol. 90, no. 5, pp. 549-573, 2006.

[49] J. G. Huddleston et al., "Characterization and comparision of hydrophilic and hydrophobic room temperature ionic liquids incorprating the imidazolium cation.," *Green Chemistry,* vol. 3, no. 4, pp. 156-164, 2001.

[50] C. D. Tran, S.H. De Paoli Lacerda and D. Oliveira, "Absorption of water by room-temperature ionic liquids: effect of anions on concentration and state of

water," *Applied Spectroscopy,* vol. 57, no. 2, pp. 152-157, 2003.

[51] M. Palacio and B. Bhushan, "A review of ionic liquids for green molecular lubrication in nanotechnology," *Tribology Letters,* vol. 40, no. 2, pp. 249-268, 2010.

[52] M. Dobbelin, R. Tena-Zaera, R. Marcilla, J. Iturri, S. Moya, J. A. Pomposo and D. Mecerreyes, "Multiresponsive PEDOT-Ionic liquid materials for the design of surfaces with switchable wettability," *Advanced Functional Materials,* vol. 19, no. 20, pp. 3326-3333, 2009.

[53] K. A. Mauritz and R. B. Moore, "State of understanding of Nafion," *Chemical reviews,* vol. 104, no. 10, pp. 4535-4586, 2004.

[54] Toolbox, The Engineering, "Viscosity of water at temperatures between 0 - 100°C (32 - 212°F) in Imperial and SI Unit," The Engineering Toolbox, http://www.engineeringtoolbox.com/water-dynamic-kinematic-viscosity-d_596.html.

[55] M. Taborelli, "Cleaning and surface properties," http://cds.cern.ch.